Three-Dimensional Structure of Convectively Coupled Equatorial Waves in Aquaplanet Experiments with Resolved or Parameterized Convection🖉

Rosimar Rios-Berrios🆔,[a] Falko Judt,[a] George Bryan,[a] Brian Medeiros,[a] and Wei Wang[a]

[a] *National Center for Atmospheric Research, Boulder, Colorado*

ABSTRACT: Accurate simulations of convectively coupled equatorial waves (CCEWs) are key to properly forecasting rainfall and weather patterns within (and outside) the tropics. Many studies have shown that global numerical weather prediction (NWP) models usually do not accurately simulate CCEWs; however, it is unclear if this problem can be alleviated with a better representation of deep convection in the models. To this end, this study investigates the representation of multiple types of CCEWs in the Model for Prediction Across Scales-Atmosphere (MPAS-A). The simulated structure of CCEWs is analyzed from three MPAS-A aquaplanet experiments with horizontal cell spacing of 30, 15, and 3 km, respectively. Using a wave-phase composite technique, the simulated structure is compared against observed CCEWs as represented by satellite and reanalysis data. All aquaplanet experiments capture the overall structure of gravity wave–type equatorial waves (e.g., Kelvin waves and inertio-gravity waves). Those waves are more realistic in the 3-km experiment, particularly in terms of the vertical structure of temperature, water vapor, and wind anomalies associated with the waves. The main reason for this improvement is a more realistic diabatic heating profile; the experiment with resolved convection produces stronger heating (or weaker cooling) below the melting level during the convectively active phase of Kelvin and inertio-gravity waves. Intriguingly, the rainfall and lower-tropospheric structure associated with easterly waves show pronounced discrepancies between the aquaplanet experiments and reanalysis. Resolved deep convection primarily affects the intensity and propagation speeds of these waves.

KEYWORDS: Inertia-gravity waves; Kelvin waves; Numerical analysis/modeling; Cloud resolving models; Model comparison; Tropical variability

1. Introduction

Convectively coupled equatorial waves (CCEWs) are important sources of tropical rainfall variability. These waves are responsible for 10%–60% of the rainfall variability in equatorial South America and equatorial Africa (Schlueter et al. 2019; Dominguez et al. 2020), and they can explain even higher rainfall variability over the tropical oceans (Kiladis et al. 2009). Some of these waves can facilitate the formation of hazardous weather, including tropical cyclones (Frank and Roundy 2006; Ventrice et al. 2012; Schreck 2015). Predicting the propagation, growth, and maintenance of CCEWs is key to accurately predicting rainfall and weather patterns within and outside the tropics. However, global numerical weather prediction (NWP) models are deficient at predicting the propagation of equatorial waves even when their structures are appropriately represented in the initial conditions (Dias et al. 2018). Some models have inadequate rainfall–kinematics phasing, which results in rainfall production in an erroneous location within the wave envelopes (Dias et al. 2018; Rios-Berrios et al. 2020b). It is commonly assumed that these issues are caused by deficiencies in the cumulus parameterization used by global NWP models (Frierson 2007; Liu et al. 2010; Straub

et al. 2010; Frierson et al. 2011; Nakajima et al. 2013; Dias et al. 2018; Weber et al. 2020). This manuscript aims at understanding how the representation of convection—specifically, whether resolved or parameterized—affects the simulated structure of CCEWs in a global model.

Studies have begun to show that resolved deep convection (i.e., explicitly representing convection with a model's governing equations and no cumulus parameterization) significantly improves the representation of CCEWs in global models (Weber et al. 2020; Judt and Rios-Berrios 2021; Rios-Berrios et al. 2022). Using the Model for Prediction Across Scales-Atmosphere (MPAS-A), Weber et al. (2020) examined a convectively coupled Kelvin wave in a simulation with parameterized convection (15-km cell spacing) and a simulation with resolved deep convection (3-km cell spacing). The 3-km simulation captured a more accurate Kelvin wave structure due to a better moisture–rainfall relationship than the simulation with parameterized deep convection. Judt et al. (2021) also examined the representation of CCEWs in MPAS-A by means of 40-day forecasts from a "horizontal resolution ensemble" with cell spacing ranging from 480 to 3.75 km. Predicted rainfall rates associated with CCEWs—especially small-scale waves—were more accurately predicted when convection was explicitly resolved. Judt et al. (2021) further demonstrated that explicitly resolving convection is more important than horizontal resolution alone because their sensitivity experiments with 3.75- and 7.5-km cell spacing *and* a convection parameterization produced similar forecasts to the experiments with 15-km cell spacing or larger. A more in-depth investigation is needed because Weber et al. (2020) examined a single

---

Corresponding author: Rosimar Rios-Berrios, rberrios@ucar.edu

CCEW and Judt and Rios-Berrios (2021) did not compare the simulated CCEWs structure among their simulations. Furthermore, it is unclear if their findings can be generalized because both studies considered single forecasts for a relatively short time period.

One way to generalize the representation of CCEWs in global NWP models is using an aquaplanet framework (Frierson 2007; Frierson et al. 2011; Blackburn et al. 2013; Nakajima et al. 2013; Nasuno et al. 2008; Blanco et al. 2016a,b). While this framework is a highly idealized representation of Earth's climate system, aquaplanet simulations are used to test how physical processes are represented in models in comparison to simple theoretical models and complex observations (Blackburn and Hoskins 2013). Their relatively long integration period also allows to statistically analyze the representation of weather phenomena in the underlying model. CCEWs are spontaneously triggered in the aquaplanet framework, but the precise waves that are simulated depend on the NWP model. For example, Nakajima et al. (2013) compared tropical rainfall variability simulated by 17 models, and the results ranged from models that simulated various types of CCEWs to models that did not simulate zonally propagating systems at all. Rios-Berrios et al. (2020b) showed that substantial variability still exists among more recent and upgraded versions of those models. Rios-Berrios et al. (2020b) also demonstrated that the aquaplanet configuration in MPAS-A captures CCEWs, including Kelvin waves, inertio-gravity waves, and easterly waves. In a follow-up study, Rios-Berrios et al. (2022) showed that CCEWs were stronger when deep convection was explicitly resolved. The precise reasons for this result remain to be investigated.

Another issue that should be investigated is whether the representation of certain types of CCEWs is more sensitive than others to the representation of convection. Adames et al. (2019) proposes that CCEWs can be classified as either gravity-type waves, moisture modes, or a combination of both. The main difference between these wave types is the dominant source of thermodynamic variability. Gravity-type waves respond more to temperature fluctuations, whereas moisture modes are driven primarily by water vapor fluctuations. Studies suggest that the Madden–Julian oscillation, equatorial Rossby waves, and eastern Pacific easterly waves can be classified as moisture modes, whereas Kelvin waves and inertio-gravity waves are better described as gravity-type waves (Adames et al. 2019; Wolding et al. 2020; Ahmed et al. 2021). Investigating whether moisture modes or gravity-type waves are more sensitive to the representation of convection in NWP models could guide future improvements of tropical rainfall predictions.

The purpose of this manuscript is twofold: 1) we aim at investigating how accurate is the simulated structure of CCEWs in aquaplanet experiments using MPAS-A, and 2) we also seek to document the impacts of resolved versus parameterized convection on the simulated structure of various CCEWs. Section 2 describes those simulations and the composite technique applied to observed and simulated CCEWs. Section 3 presents the results from our aquaplanet experiments and compares them against reanalysis and satellite data. Last, section 4 provides conclusions about this study.

2. Methods

a. Experimental setup

We examined CCEWs as simulated by MPAS-A, which is a global, nonhydrostatic model that uses C-grid discretization on an unstructured Voronoi mesh (Skamarock et al. 2012). This framework allows for either a global mesh with quasi-uniform cells or for a variable-resolution mesh with small cells in a region of interest transitioning to larger cells outside that region. Both configurations were used in this study to produce simulations with different horizontal resolutions, with an emphasis on tropical weather.

Our MPAS-A aquaplanet experiments are described in detail in Rios-Berrios et al. (2020b, 2022); therefore, we only provide a short summary here. The aquaplanet configuration largely followed the protocol of the Aqua-Planet Experiment (APE; Williamson et al. 2013). The model domain was configured as a water-covered sphere with a surface boundary condition given by the "QOBS" profile from the APE [see Fig. 1a from Neale and Hoskins (2000)]. This profile yields a maximum SST of 27°C at the equator and a meridionally varying SST until reaching 0°C at 60°N/S. A caveat of this SST profile is that it might limit CCEWs that are antisymmetric with respect to the equator. Sea ice was not allowed to form. The model included diurnal insulation but no seasons (i.e., perpetual equinox) and no radiatively active aerosols. The ozone distribution was given by a hemispheric-symmetric dataset provided by the APE.

We present results from three aquaplanet experiments: two experiments with uniform meshes and one experiment with a variable-resolution mesh. The two experiments with uniform meshes used 30- and 15-km horizontal cell spacing. These experiments employed the new Tiedtke convection parameterization (Zhang and Wang 2017); therefore, we will refer to them as the "parameterized convection experiments." The third experiment used 3-km cell spacing between 20°S and 20°N, 15-km cell spacing poleward of 30°N and 30°S, and a transition zone in between. This experiment used a scale-aware version of the new Tiedtke scheme (Wang 2022), which reduces the amplitude of the parameterized convective mass flux for cell spacings below 15 km. Over 90% of the tropical rainfall is explicitly resolved in this experiment while less than 10% is parameterized (not shown); therefore, we will refer to this experiment as the "resolved convection experiment." The time steps and diffusion length scales were adjusted accordingly for each experiment (see Table 1 of Rios-Berrios et al. 2022). All experiments had 75 vertical levels with a model top at 40 km. The experiments also used the following model physics: WRF single-moment six class microphysics (Hong et al. 2006), Yonsei University boundary and surface layer schemes (Hong et al. 2004), and the Rapid Radiative Transfer Model for GCMs (RRGTM; Iacono et al. 2008) for both shortwave and longwave radiation with modifications for perpetual equinoctial conditions. The analysis is based on the last 100 days of each simulation.

b. Analysis

The 100-day period captures CCEWs as demonstrated by the wavenumber–frequency spectral analysis shown on Fig. 1.
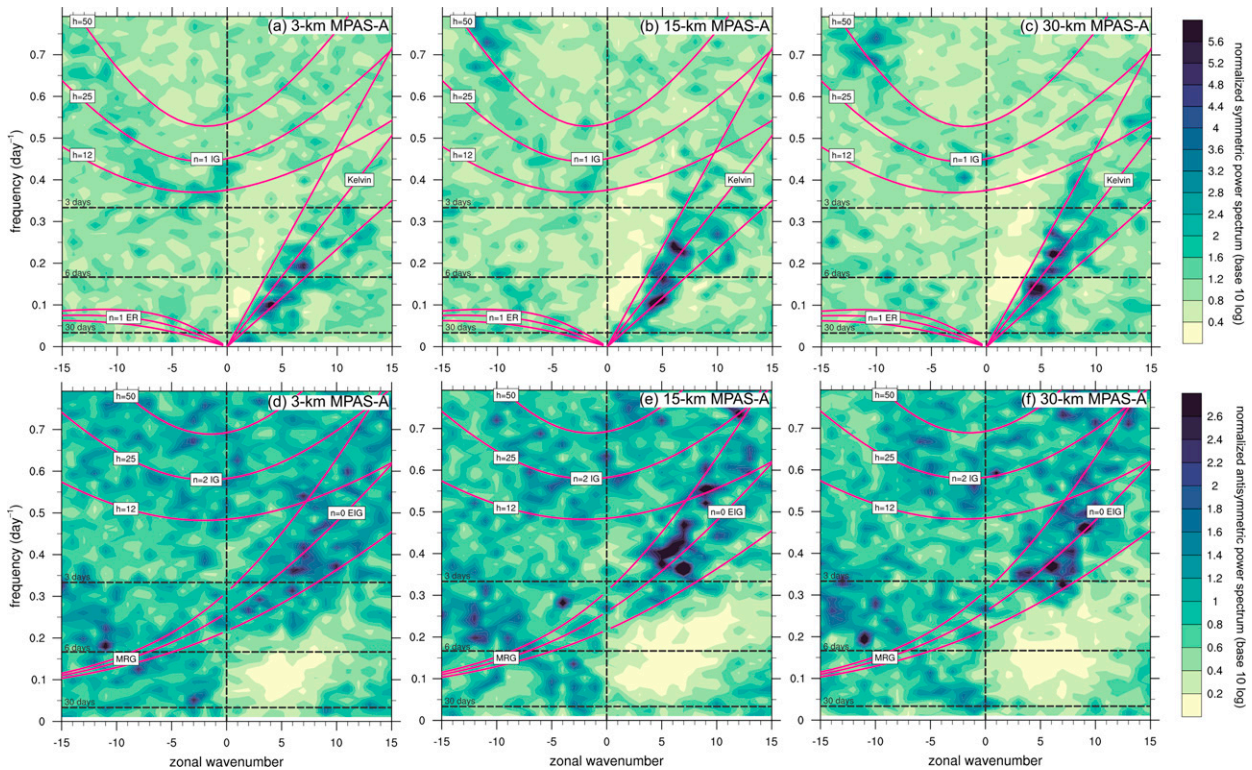
FIG. 1. Wavenumber–frequency normalized power spectrum (shading; base 10 log) of the (top) symmetric and (bottom) antisymmetric components of rainfall rate between 10°S and 10°N. Panels show the (a),(d) 3-; (b),(e) 15-; and (c),(f) 30-km experiments. Magenta lines depict the theoretical dispersion relationships for different convectively coupled equatorial waves.

This analysis was done on 6-hourly rainfall rates between 10°N and 10°S following the steps of Wheeler and Kiladis (1999). As documented by Rios-Berrios et al. (2020b), Kelvin waves appear in the aquaplanet framework using MPAS-A regardless of horizontal resolution (Figs. 1a–c). The $n = 0$ and 1 inertio-gravity waves are also active in this framework, but their spectral peaks appear at a narrower frequency window in the experiments with parameterized convection (Figs. 1d–f). The power spectrum associated with Kelvin waves is approximately twice as strong as the spectrum associated with antisymmetric waves, which is likely a result of the symmetric SST profile. There is also an additional spectral signal that spans the characteristic wavenumbers and frequencies of equatorial Rossby waves and easterly waves. This peak appears in both the symmetric and antisymmetric components (although the symmetric component is partially overshadowed by the larger power spectra associated with Kelvin waves). This additional signal has been previously identified on aquaplanet experiments by Nakajima et al. (2013), who attributed it to "advective disturbances." Only the 3-km experiment shows a weak signal likely associated with the Madden–Julian oscillation (MJO), but the simulation length (100 days) is likely too short to capture enough MJO events (with periods between 30 and 90 days).

This study focuses on three types of CCEWs: Kelvin waves, westward-propagating inertio-gravity waves, and easterly waves. The corresponding wave definitions for these waves are as follows:

- Kelvin waves are eastward-propagating disturbances spanning wavenumbers 1–14 and periods of 2.5–20 days,
- westward-propagating inertio-gravity waves (inertio-gravity waves hereafter) are westward-propagating disturbances spanning wavenumbers 1–15 and periods of 1.8–4.5 days, and
- easterly waves are westward-propagating disturbances spanning wavenumbers 6–28 and periods of 2.5–7.0 days.

Each wave type was identified using spatiotemporal filtering on latitudinally averaged rainfall between 10°S and 10°N. The inertio-gravity waves group include both $n = 1$ and 2 waves, but their combined signal is likely dominated by the $n = 1$ waves because the latitudinal averaging masks out some of the asymmetries of $n = 2$ waves.

1) COMPARISON WITH OBSERVED WAVES

We compared the simulated structure of CCEWs against their observed structured as represented by satellite and reanalysis data. Precipitation estimates were obtained from NASA's Integrated Multi-satellitE Retrievals for GPM (IMERG; Huffman et al. 2019). Rainfall rates are estimated from satellite radar and infrared measurements, which are combined into a 0.1° × 0.1° gridded dataset. We used the 30-min final product from IMERG and used conservative interpolation to regrid the data to 6-hourly rainfall rates onto a 0.25° × 0.25° grid. This resolution matches the resolution of the atmospheric fields, which were obtained from the fifth-generation ECMWF

reanalysis (ERA5; Hersbach et al. 2020). The 6-hourly rainfall rates and atmospheric fields were obtained for each day, where the rainfall rates represent the average rates within a 6-h period and the atmospheric fields represent instantaneous quantities at the center of the rainfall time period. This choice allows analyzing the atmospheric conditions associated with—rather than preceding or following—the rainfall patterns.

We analyzed observed CCEWs at all seasons between 2001 and 2020. All these years have a complete annual dataset from both IMERG and ERA5 (IMERG begins in late 2000). To minimize the effects of seasonality and to make a fair comparison with the aquaplanet framework, we removed the annual and seasonal cycles from all the fields discussed here. The annual and seasonal cycles were calculated by first averaging the fields every 6 h from 0000 UTC 1 January to 1800 UTC 31 December (including 29 February), and then retaining the first three harmonics of those averages. CCEWs were then identified with a spatiotemporal filter using the same wavenumbers and frequencies as in the aquaplanet simulations. An examination of wave-filtered climatological variance showed that the three groups of CCEWs are active over the Pacific Ocean (not shown), where the aquaplanet framework is also most similar to Earth. Therefore, the analysis of IMERG and ERA5 focused on CCEWs over water between 10°S and 10°N and between 150° and 270°E.

2) WAVES IDENTIFICATION AND COMPOSITE TECHNIQUE

We used a *wave phase composite technique* to analyze the observed and simulated CCEWs. This approach was inspired by several studies that conducted multiyear surveys of CCEWs (Riley et al. 2011; Yasunaga and Mapes 2012; van der Linden et al. 2016; Schlueter et al. 2019; Sakaeda et al. 2020). Figure 2 shows an example of this approach using IMERG data. To determine the wave phases, first rainfall rates were averaged within 10°S–10°N in the aquaplanet experiments and within 5°S–5°N in IMERG.[1] Those latitudinally averaged rainfall rates were then filtered in time and space for each wave (see e.g., Fig. 2a). Next, the filtered rainfall and its time derivative were normalized by their standard deviations at each longitude. The normalized quantities were sorted into a phase space as illustrated in Fig. 2b, assigning each longitude–time coordinate to a corresponding wave phase. We then matched the unfiltered precipitation and dynamical fields from each longitude–time coordinate to their corresponding location in the wave phase space.

We split the wave phase into 45 bins and averaged each field within those bins, but for simplicity, only eight phases will be used in the discussion and figures. Phase 5 corresponds to the convectively active phase and phase 1 corresponds to

the convectively inactive phase. We considered only data points where the norm of the normalized tendency and its anomaly was greater than one standard deviation in MPAS-A and two standard deviations in IMERG to retain "strong" waves. This criterion was satisfied by 55%–60% of MPAS-A and 12%–13% of IMERG data points depending on the wave type; this stark difference highlights the favorability for CCEW activity in the MPAS-A aquaplanet configuration. Last, the mean from all wave phases was removed from the fields to show field anomalies as a function of wave phase.

Figure 2c demonstrates that this composite technique works well for any wave. This figure shows composite rainfall rate anomalies corresponding to Kelvin waves, inertio-gravity waves, and easterly waves between 2001 and 2020 and within the Pacific Ocean domain described above. These anomalies are *not filtered*; they correspond to the sorted rainfall rates as a function of wave phase. There is a clear wave structure in the anomalies; rainfall peaks happen at wave phase 5 and rainfall minima happen at wave phase 1. A benefit of using this method is that it can be equally applied to observations and model data, as will be shown below. Another benefit is that all waves are grouped together into a phase space that captures the entire life cycle of the waves.

3. Results

a. Kelvin waves

1) RAINFALL, CLOUDS, AND HORIZONTAL STRUCTURE

To investigate the representation of Kelvin waves in MPAS-A, we first examine the horizontal structure of key quantities modulated by these waves. Figure 3 shows latitude–wave phase composites of rainfall rate anomalies, column-integrated cloud water (including both condensate and ice), and wind anomalies at 850 and 200 hPa. As a reminder, the composites are based on raw (i.e., unfiltered) fields that are sorted and averaged as a function of wave phase. The MPAS-A analysis focuses on the 3- and 15-km experiment because the two experiments with parameterized convection are very similar to each other.

The 20-yr composite from IMERG shows the heaviest rainfall at around 7.5°N with lighter rainfall extending from ~10°S to at least ~10°N (Fig. 3a). The column-integrated cloud water also exhibits the largest anomaly in the Northern Hemisphere between phases 4 and 6 (Fig. 3d). These asymmetries appear because most Kelvin waves happen along the ITCZ, which climatologically is located in the Northern Hemisphere (Berry and Reeder 2014). The 20-yr wind composites from ERA5 show anomalous lower-tropospheric easterlies between phases 5 and 8 and westerlies between phases 1 and 5 (Fig. 3a). There are also anomalous upper-tropospheric westerlies between phases 5 and 8 and easterlies between phases 1 and 4 (Fig. 3d). Converging lower-tropospheric winds happen around wave phase 5 or slightly east of the heaviest rainfall; diverging upper-tropospheric winds happen between phases 4 and 5 or to the west of the heaviest rainfall. Overall, the composite technique with

---

[1] The different choice of latitudinal band was made because the tropical belt in the aquaplanet experiments extends farther poleward from the equator than in observations. Using a latitudinal averaging between 10°S and 10°N in IMERG resulted in more asymmetric structures about the equator that are difficult to compare against the symmetric configuration from the aquaplanet framework.
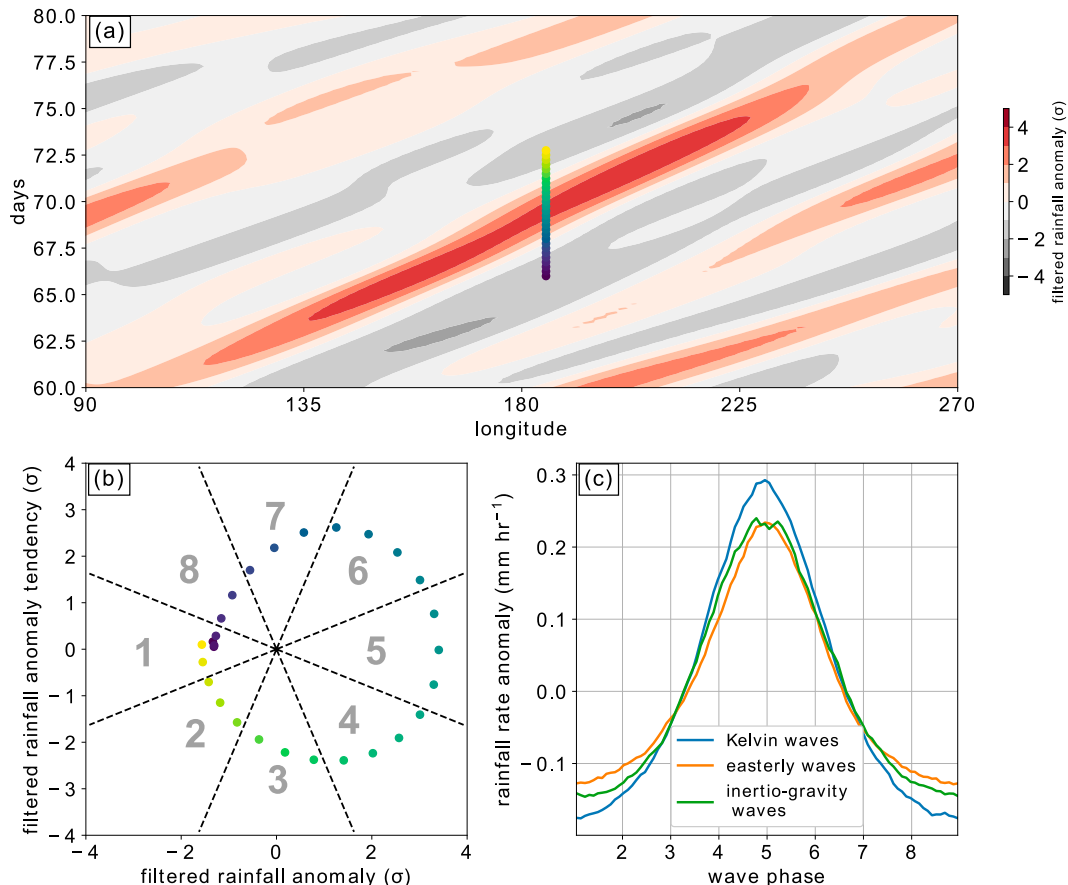
FIG. 2. Example of the wave identification and composite technique used in this study. (a) The 6-hourly filtered rainfall (shading; every 1 mm h^{-1}) for Kelvin wave frequencies and wavelengths in an MPAS-A aquaplanet simulation. The colored dots in (a) correspond to different 6-hourly output times and are also plotted in (b) on their corresponding filtered rainfall anomaly tendency and filtered rainfall anomaly. (b) The two-dimensional wave-phase space, which is divided into octants to yield eight wave phases (indicated by the gray numbers), and the same dots as in (a). (c) The composite rainfall anomaly for Kelvin (blue), easterly (orange), and inertio-gravity (green) waves as a function of wave phase.

IMERG and ERA5 captures the expected structure of lower-tropospheric easterlies to the east of convection, and upper-tropospheric easterlies to the west of convection (Straub and Kiladis 2003; Roundy 2008; Kiladis et al. 2009). We will use this climatological composite as a benchmark to evaluate the structure of simulated Kelvin waves.

Our MPAS-A aquaplanet simulations show a different Kelvin wave structure depending on whether convection is mostly resolved or parameterized. The 3-km experiment has the strongest rainfall rates between phases 5 and 6, collocated with converging lower-tropospheric winds and diverging lower-tropospheric winds (Figs. 3b,e). This overall pattern is consistent with the observed structure of Kelvin waves, although rainfall rates peak at or near the equator in the aquaplanet simulations in response to the prescribed symmetric SST profile. The heaviest rainfall rate anomalies are mostly confined to 5°S–5°N, with regions of precipitation extending poleward and westward from the heaviest rainfall. This "arrowhead"

structure[2] is more pronounced than in the IMERG composite, and it resembles the Gill response to symmetric heating at the equator (Gill 1980). Although not shown here, the poleward rainfall anomalies are likely associated with westward-propagating disturbances that initiate after the Kelvin wave peak only in the 3-km experiment. The cloud field is very similar in structure to the rainfall rates, suggesting strong coupling between clouds and rainfall when deep convection is resolved (Figs. 3b,e). The simulations with parameterized deep convection show a slightly different structure than the experiment with resolved deep convection. In particular, the 15-km experiment exhibits weaker

---

[2] The "arrowhead" structure resembles the structure of the MJO (e.g., Adames and Wallace 2015). It is possible that a few MJO events appear in the 3-km experiment and project onto the Kelvin wave composites. However, it is difficult to confirm this possibility because the analysis period only extends for 100 days whereas the typical time periods of MJO events are 30–90 days.
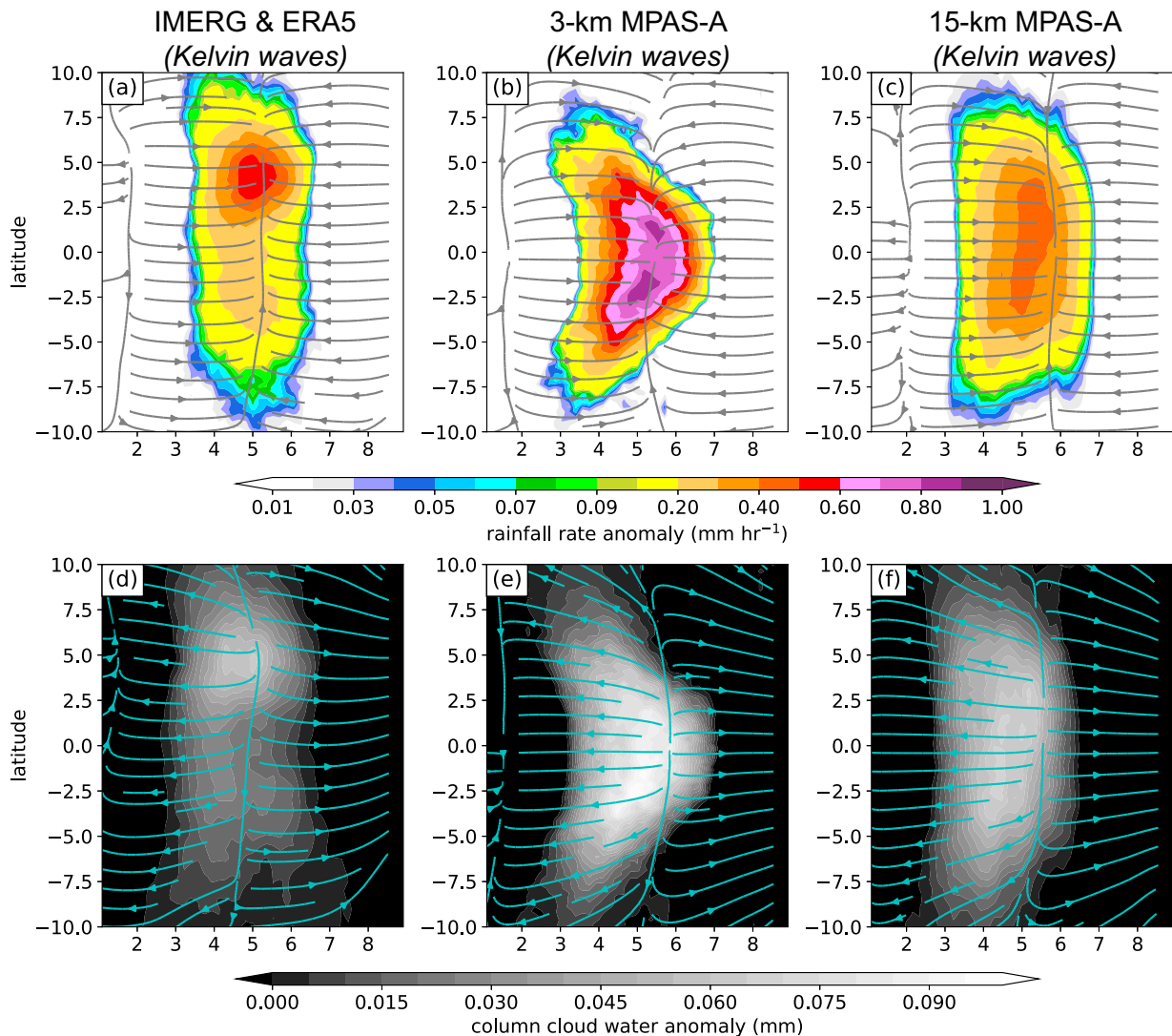
FIG. 3. Latitude–wave phase composites for Kelvin waves showing (top) anomalous precipitation rate (shading) and 850-hPa horizontal winds and (bottom) anomalous column-integrated cloud water and 200-hPa horizontal winds. The composites from (a),(d) IMERG (rainfall rates) and ERA5 (winds); (b),(e) the 3-km MPAS-A aquaplanet experiment; and (c),(f) the 15-km MPAS-A aquaplanet experiment. The composites are sorted by wave phase, where phase 5 is the convectively active phase.

rainfall rate anomalies and a broader rainfall shield (spanning 10°S–10°N) than in the 3-km experiment (Figs. 3c,f).

Importantly, the lower-tropospheric and upper-tropospheric winds are notably different between these experiments. The 3-km experiment shows anomalous lower-tropospheric easterly winds between phases 5 and 1 and westerlies between phases 2 and 4 in collocation with much of the rainfall shield (Figs. 3b). Peak lower-tropospheric convergence happens around phase 5, which is around the region of heaviest rainfall rate anomalies and is also consistent with ERA5. The upper-tropospheric winds also exhibit the expected structure with anomalous westerlies around phases 6–1 and anomalous easterlies in the other phases (Figs. 3e). In contrast, the 15-km experiment shows peak lower-tropospheric convergence around phase 6 (Figs. 3c)—eastward of both IMERG and the 3-km

experiment. Because Kelvin waves propagate eastward, this result means that the experiments with parameterized convection produce maximum rainfall to the west of the lower-tropospheric convergence. This is different than in both the resolved convection experiment and the ERA5 reanalysis. Moreover, the upper-tropospheric winds indicate that maximum divergence happens between phases 5 and 6 in the 15-km experiment (Figs. 3f), which suggests a smaller vertical tilt with height in the parameterized convection experiments.

2) VERTICAL STRUCTURE

Next, we investigate the vertical structure of Kelvin waves in ERA5 and in our MPAS-A aquaplanet simulations. We focus on key variables that characterize the thermal, dynamic,
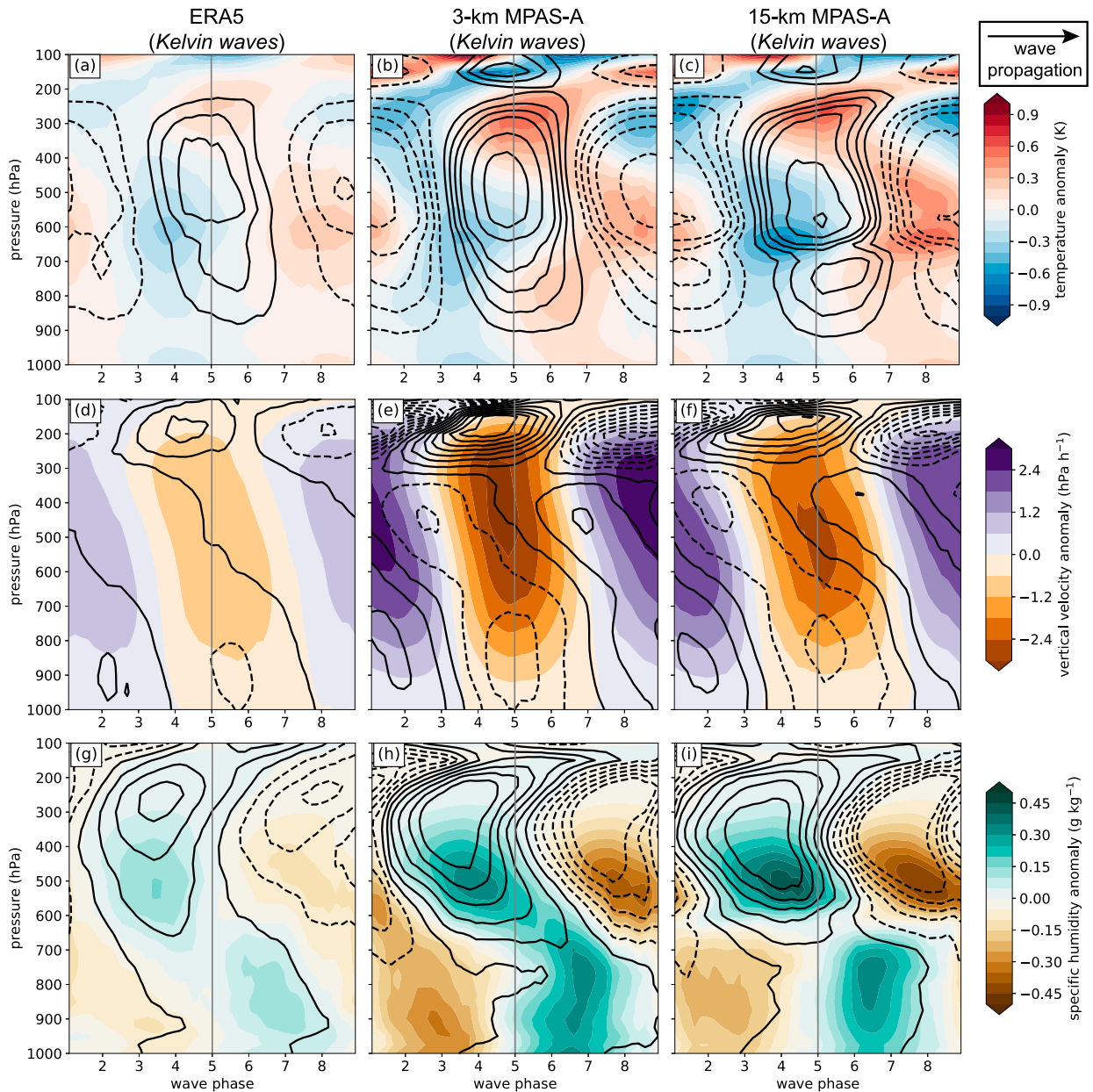
FIG. 4. (a)–(c) Pressure–wave phase composites for Kelvin waves showing anomalous temperature (shading, every 0.1 K) and apparent heat source (Q_1; contours, every 0.9 K day^{-1}) from (a) ERA-5, (b) an MPAS-A simulation with convection-permitting resolution, and (c) an MPAS-A simulation with parameterized deep convection. (d)–(f) As in (a)–(c), but for anomalous vertical velocity (shading, every 0.6 hPa h^{-1}) and divergence (contours, every 0.6 × 10^{-5} s^{-1}). (g)–(i) As in (a)–(c), but for anomalous water vapor mixing ratio (shading, every 0.05 g kg^{-1}) and relative humidity (contours, every 2%). In all panels, solid contour lines represent negative anomalies and dashed contour lines represent positive anomalies.

and moisture structure of CCEWs. Figure 4 shows pressure–wave phase (i.e., vertical cross sections) composite anomalies of those key variables averaged between 10°S and 10°N. The 20-yr ERA5 climatology shows middle and lower-tropospheric cold anomalies between phases 2 and 6 and warm anomalies between phases 6 and 1 (Fig. 4a). Warm anomalies also appear aloft (between 150 and 350 hPa) during the convectively active

phase. To relate these anomalies to the structure of diabatic heating, we examined the apparent heat source or Q_1 (Yanai et al. 1973). The Q_1 was calculated as the residual from the dry static energy (s) equation:

$$Q_1 = \frac{\partial s}{\partial t} - u\frac{\partial s}{\partial x} - v\frac{\partial s}{\partial y} - \omega\frac{\partial s}{\partial p}, \qquad (1)$$

where $s = c_p T + gz$, u is the zonal wind, v is the meridional wind, and ω is the vertical velocity. This field exhibits a vertical tilt with height in ERA5, such that anomalous heating begins in the boundary layer around phases 7–8 and maximizes in the middle to upper troposphere between phases 4 and 6 (over and west of the rainfall peak) (Fig. 4a). Deep-tropospheric heating exists during phase 5 (this is known as the first baroclinic mode). Anomalous cooling happens mostly over the convectively inactive phases (phases 7–3).

Other key fields also exhibit a vertical tilt with height in ERA5. The vertical motion exhibits anomalous ascent east of the rainfall peak (phase 6) in the lower troposphere, over the rainfall peak (phase 5) in the middle troposphere, and west of the rainfall peak (phases 3–4) in the upper troposphere (Fig. 4d). This structure resembles the well documented transition from shallow to deep convection to stratiform precipitation in Kelvin waves (Straub and Kiladis 2003). The divergence fields shows anomalous lower-tropospheric convergence between phases 5 and 7, which is over and east of the rainfall peak (Fig. 4d). Anomalous upper-tropospheric divergence appears between phases 3 and 5, which is over and west of the convective peak. The moisture fields of ERA5 also exhibit a vertically tilted structure (Fig. 4g). The specific humidity shows two regions of peak moist anomalies: a lower-tropospheric peak around 700–900 hPa between phases 6 and 8 and a middle-tropospheric peak around 500 hPa between phases 3 and 5. The relative humidity exhibits a single upper-tropospheric peak around 300 hPa between phases 3 and 5, which is likely an imprint of elevated nimbostratus clouds (Roundy 2008). Anomalously dry conditions happen in the lower troposphere west of the rainfall peak (phases 1–5), while dry conditions in the middle and upper troposphere happen to the east of the rainfall peak (phases 6–1).

All simulations capture (to some extent) the general structure of Kelvin waves, with some noteworthy differences from the climatology. The anomalies calculated from MPAS-A are stronger in magnitude than those from ERA5 (Fig. 4), but this difference could be due to a number of factors including the different sample sizes, the background conditions taken for the anomalies, or absence of many features in the aquaplanet. Nonetheless, the aquaplanet simulations exhibit a baroclinic structure with alternating cool and warm anomalies with height (Figs. 4b,c). All simulations also capture a vertically tilted structure of diabatic heating, ascent, and divergence (Figs. 4a–f). The vertical tilt is slightly more pronounced in the 3-km experiment than in the other experiments. Peak moist and dry anomalies appear in the middle to upper troposphere, but the lower-tropospheric moist and dry anomalies exhibit almost no vertical tilt in MPAS-A (Figs. 4h,i).

Resolved deep convection affects key features of the vertical structure of simulated Kelvin waves. The most evident effects appear in the temperature, Q_1, and water vapor mixing ratio. The parameterized convection experiments have stronger temperature anomalies between 600 and 700 hPa than both the 3-km experiment and ERA5 (Figs. 4a–c). There is also drier air within that layer, which essentially decouples the lower-tropospheric and upper-tropospheric moisture anomalies. The parameterized convection experiments also have an "inflection" in Q_1. Such inflection is more evident in Fig. 5,
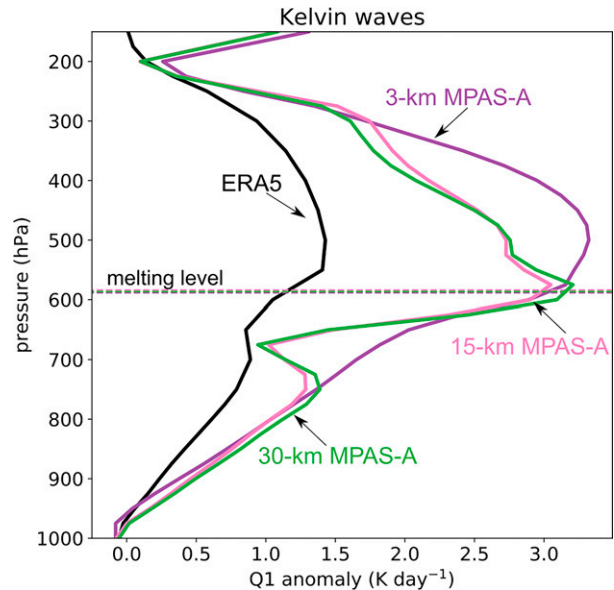

FIG. 5. Vertical profiles of composite anomalous Q_1 during phases 4–6 of Kelvin waves ERA5, (solid, dashed) and the 30-km (green), 15-km (pink), and 3-km (purple) MPAS-A aquaplanet experiments. Dashed horizontal lines mark the freezing level on each dataset.

which shows Q_1 anomalies averaged between phases 4 and 6. The experiments with parameterized convection (green and pink lines) have a sharp reduction with a relative minimum of approximately 1 K day^{-1} located around 675 hPa. While Q_1 is expected to have an inflection below the melting level (Johnson et al. 2016), the inflection is much stronger in the parameterized convection experiments than in both the 3-km experiment and ERA5. This result suggests that the convection parameterization is producing too much melting of hydrometeors.

Figure 5 also highlights how Q_1 reaches a stronger peak at a higher altitude in the 3-km experiment than in both ERA5 and the parameterized convection experiments. Kelvin waves in the 3-km experiment are associated with peak anomalous heating of up to 3.5 K day^{-1} between 400 and 500 hPa, but the anomalous heating of the 30- and 15-km experiment peaks around 600 hPa and the Q_1 anomalies from ERA5 only reach up to 1.5 K day^{-1} within that layer.

Another key difference between the experiments is the location and strength of peak anomalous ascent. Consistent with Q_1, vertical velocity peaks at different altitudes whether convection is parameterized or resolved; that peak happens around 200–400 hPa in the 3-km experiment but around 450–650 hPa in the 15-km experiment (Figs. 4e,f).

Last, the experiment with resolved deep convection has overall stronger boundary layer convergence, wetter middle tropospheric conditions, stronger ascent and stronger upper-tropospheric divergence within the convectively active phase, and stronger descent during the convectively inactive phase than the 15-km experiment (Figs. 4e–i). All these features—in combination with the stronger rainfall rates—point at a more intense coupling between rainfall and circulation when deep convection in resolved.
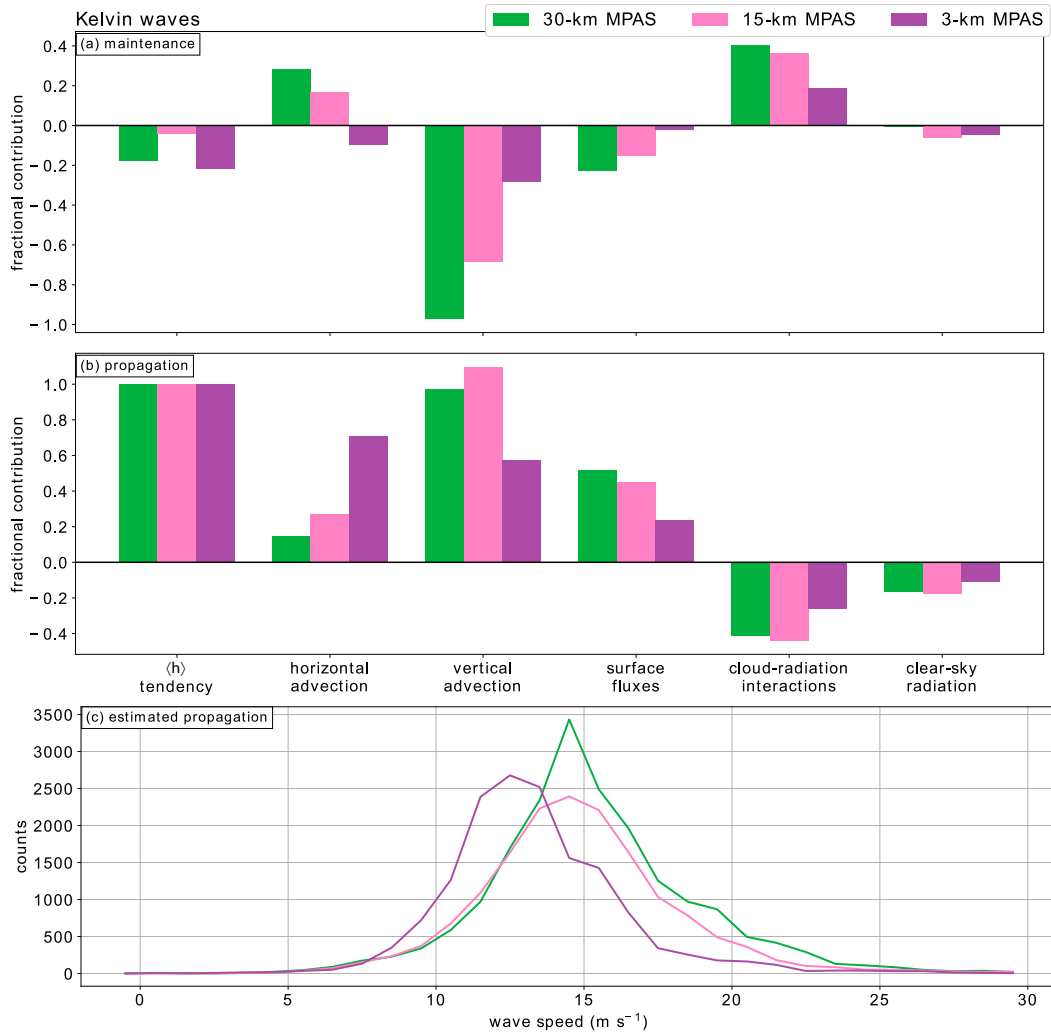
FIG. 6. (a),(b) Fractional contributions from different MSE budget terms to Kelvin wave (a) maintenance and (b) propagation in the 30-km (green), 15-km (purple), and 3-km (purple) MPAS-A experiments. (c) Binned distributions of the estimated propagation speed of Kelvin wave crests in the MPAS-A experiments.

3) MOIST STATIC ENERGY BUDGET

We use a moist static energy (MSE) budget to understand how the different vertical structure may affect the maintenance and propagation of the simulated Kelvin waves. Previous studies have examined MSE budgets to characterize the growth and maintenance of equatorial waves and the Madden–Julian oscillation (Maloney 2009; Maloney et al. 2010; Andersen and Kuang 2012; Sobel et al. 2014; Feng et al. 2020b; Nakamura and Takayabu 2022). We focus on the aquaplanet simulations for which we are able to calculate reliable MSE budgets (see supplemental material). The vertically integrated MSE budget is defined as

$$\frac{\partial \langle h \rangle}{\partial t} = -\langle \mathbf{V}_h \cdot \nabla_h h \rangle - \left\langle \omega \frac{\partial h}{\partial p} \right\rangle + \text{SF} + \text{CRI} + \text{CLEAR},$$

(2)

where h is MSE, $\mathbf{V}_h$ is the horizontal wind vector, ω is vertical velocity, SF represents surface turbulent enthalpy fluxes, CRI represents cloud-radiation interactions, CLEAR represents clear-sky radiative forcing, and the angle brackets represent a vertical integration from 1000 to 100 hPa. The terms on the right hand side represent (from left to right): horizontal MSE advection, vertical MSE advection, and the forcing terms. All terms were calculated directly from 6-hourly model output. The calculated tendency and the sum of individual terms nearly match each other (Fig. S1 in the online supplemental material), thus giving us confidence in this analysis.

We diagnosed the contributions of each term in the MSE budget to wave *maintenance* and *propagation* following Andersen and Kuang (2012). The main idea is to project the MSE budget onto $\langle h \rangle$ to quantify contributions to wave maintenance and onto the temporal tendency of $\langle h \rangle$ to quantify the contributions to wave propagation. Figures 6a
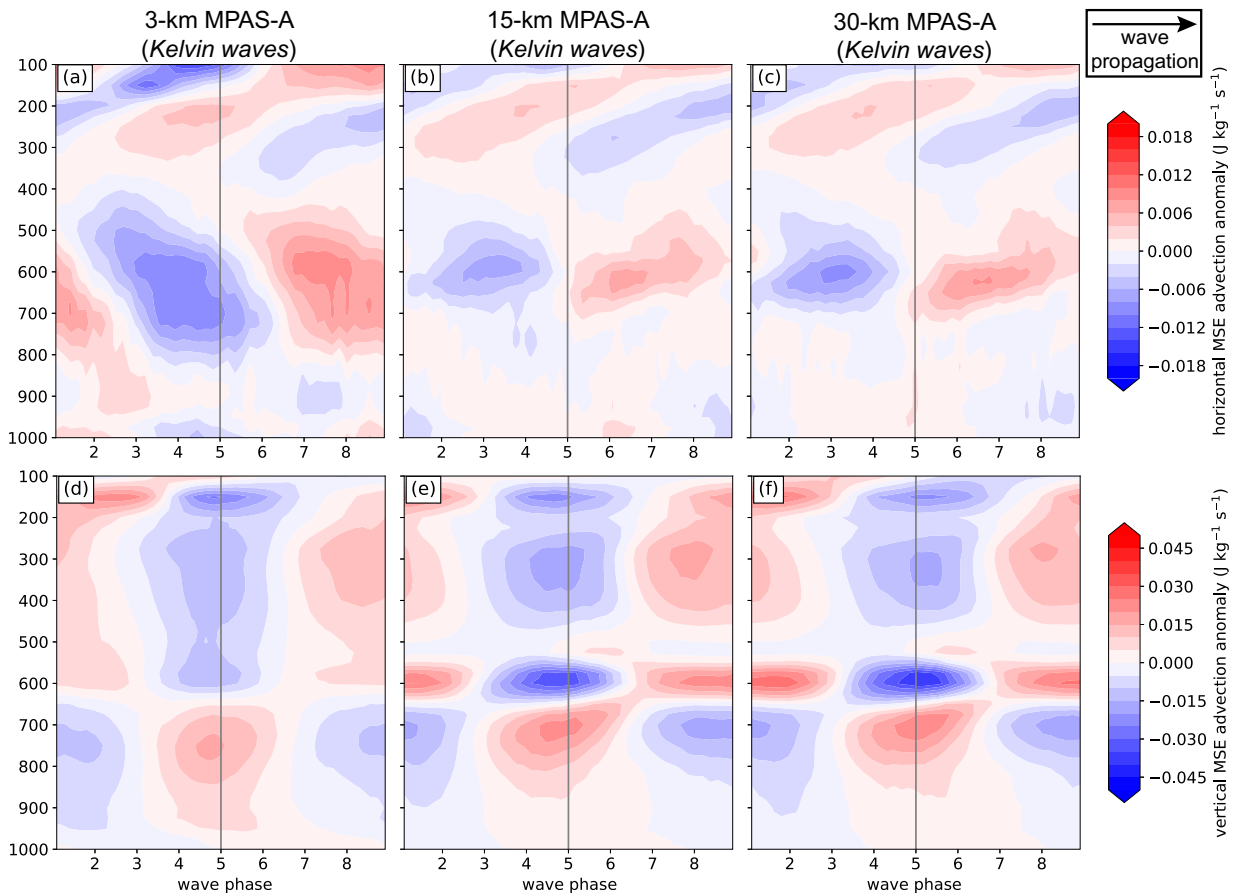
FIG 7. Pressure–wave phase composites for Kelvin waves showing anomalous (top) horizontal MSE advection and (bottom) vertical MSE advection from the (a),(d) 3-; (b),(e) 15-; and (c),(f) 30-km MPAS-A aquaplanet experiments.

and 6b shows those contributions for Kelvin waves in the different MPAS-A aquaplanet experiments. The contributions span all wave phases; on average, our analysis captures mostly decaying or nearly steady state Kelvin waves as indicated by the negative contributions from the temporal $\langle h \rangle$ tendency.

The analysis of wave maintenance shows important differences between experiments (Fig. 6a). Horizontal MSE advection, together with CRI, contribute to wave amplification (noted by positive contributions) in the experiments with parameterized deep convection. In contrast, CRI is the main amplification mechanism in the 3-km experiment. CRI supports wave amplification through a "greenhouse feedback" where clouds reduce the amount of outgoing longwave radiation, resulting in warming and moistening that can increase $\langle h \rangle$ (Andersen and Kuang 2012; Benedict et al. 2020). The smaller CRI contributions from the 3-km experiment likely result from the narrower cloud coverage as noted in Fig. 3. It is intriguing, however, that horizontal MSE advection amplifies the Kelvin waves in the 30- and 15-km experiments, but this process dampens the waves in the 3-km experiment. Furthermore, the contributions from vertical MSE advection to wave dampening are 2–3 times smaller in the 3-km experiment than in the other experiments. All other processes

contribute to wave dampening, with surface fluxes having negligible contributions in the 3-km experiment.

The contributions to wave propagation also differ across the simulations (Fig. 6b). Horizontal MSE advection, vertical MSE advection, and surface fluxes facilitate the eastward propagation of Kelvin waves, while radiative fluxes oppose their propagation in all experiments. As in the analysis of wave maintenance, the advective processes are substantially different between the MPAS-A experiments; horizontal MSE advection is the leading process contributing to propagation in the 3-km experiment, whereas vertical MSE advection is the leading process in the other experiments.

To investigate these contrasting processes, Fig. 7 shows vertical cross sections of horizontal and vertical MSE advection as a function of pressure and wave phase. The 3-km experiment has broad regions of positive and negative horizontal advection extending from 800 to 400 hPa (Fig. 7a). While the parameterized convection experiments also exhibit such dipoles, their magnitudes are weaker and their signatures span only between 700 and 500 hPa (Figs. 7b,c). These experiments also show upper-tropospheric horizontal MSE advection of opposite signs to those in the lower to middle troposphere, which results in small vertically integrated horizontal MSE advection.
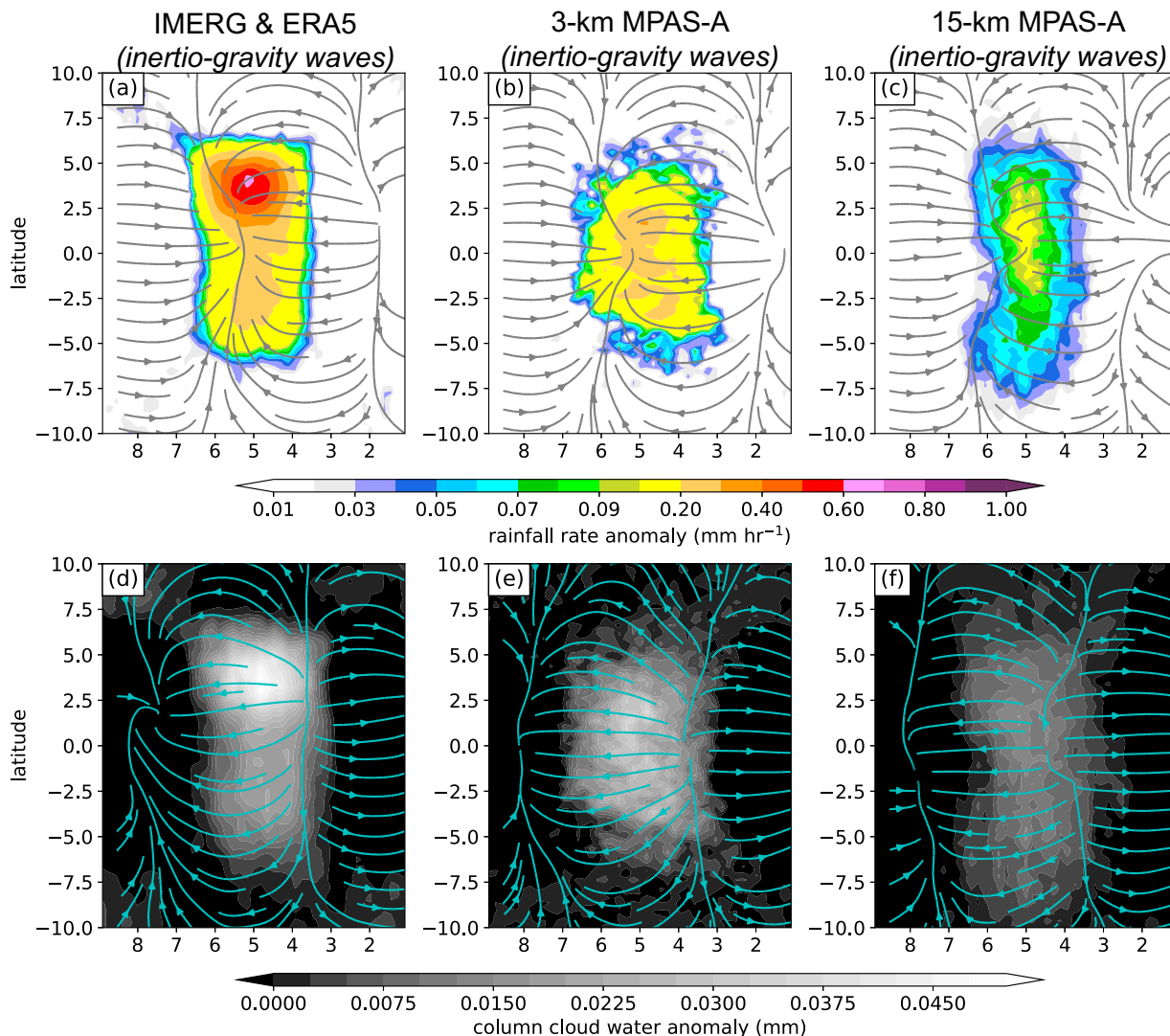
FIG. 8. As in Fig. 3, but for inertio-gravity waves.

The vertical cross sections of vertical MSE advection also exhibit pronounced differences between the experiments. The 3-km experiment is associated with positive vertical MSE advection in the lower troposphere and negative vertical MSE advection in the upper troposphere during the convectively active phase (Fig. 7d). An opposite pattern—negative values below positive values—appears in this experiment during the convectively inactive phase. The 15- and 30-km experiments exhibit pronounced dipoles below and above 650-hPa (Figs. 7e,f), which is around the same pressure level of the aforementioned discontinuities in Q_1, temperature, and water vapor anomalies (Figs. 4). The stronger negative anomalies between 600 and 500 hPa during the convectively active phase likely contribute to the stronger contributions to maintenance and propagation in these experiments than in the 3-km experiment.

The MSE budget analysis suggests that Kelvin waves may exhibit different propagation speeds in the 3-km experiment. We explored this possibility by estimating the propagation speeds of Kelvin waves in the aquaplanet experiments. Specifically, we estimated the phase speeds by calculating the 12-h centered difference of wave peaks (i.e., the location of wave phase 5). The results are shown in Fig. 6c through distributions of wave speed from each experiment binned into 1 m s^{-1} bins. This analysis confirms that Kelvin waves exhibit different propagation speeds; Kelvin waves propagate slower when deep convection is explicitly resolved. The distribution from the 3-km experiment is shifted toward lower values, resulting in an average propagation speed of 13 m s^{-1} in the 3-km experiment and ~14.7 m s^{-1} in the other experiments. A more detailed analysis is needed to confirm how the Kelvin waves propagation is
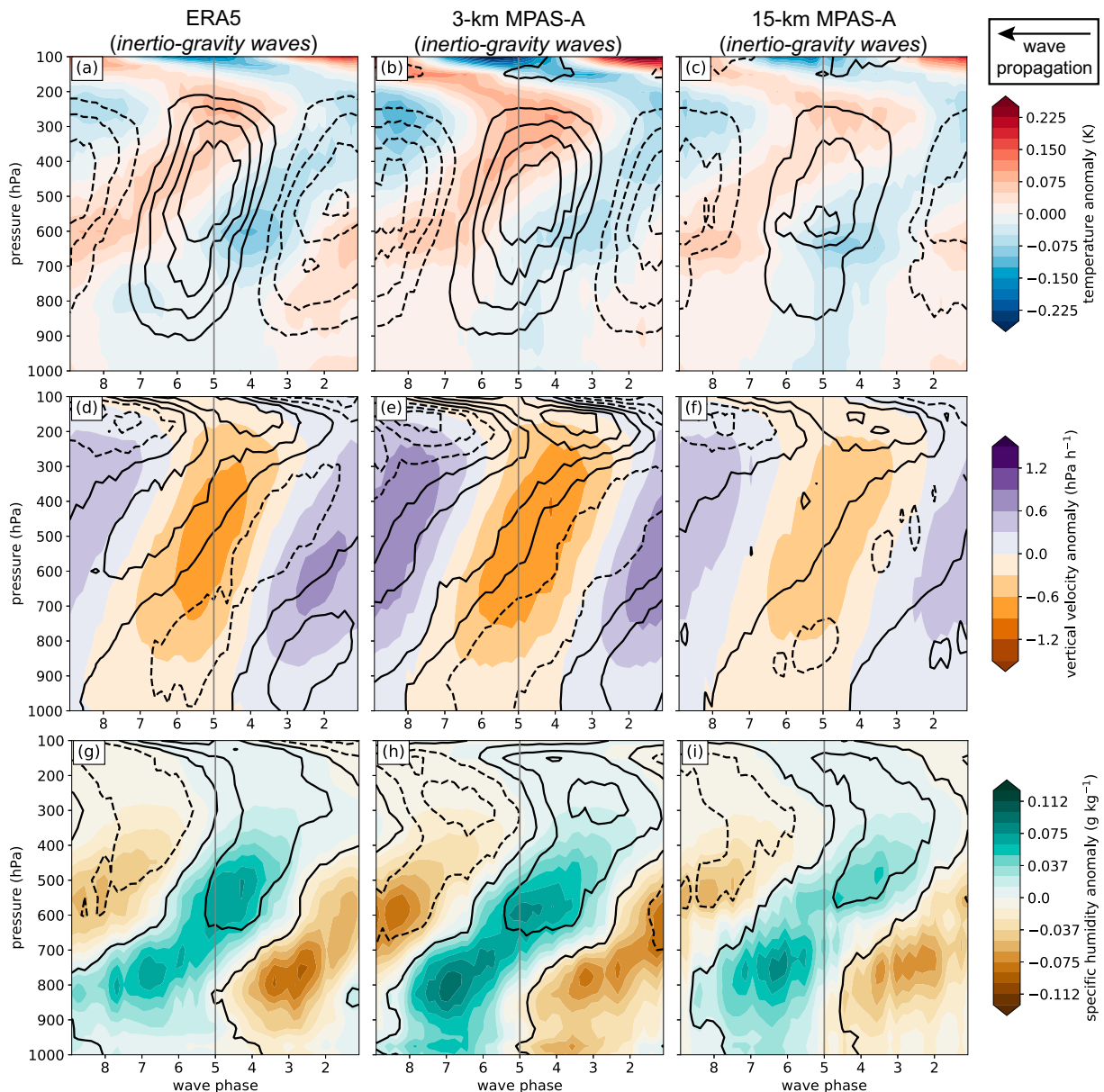
FIG. 9. As in Fig. 4, but for inertio-gravity waves.

affected by interactions between the different mean states and wave structures resulting from resolved convective-scale processes in the 3-km experiment.

b. Inertio-gravity waves

1) RAINFALL, CLOUDS, AND HORIZONTAL STRUCTURE

In this section we present the analysis of inertio-gravity waves. All plots use a reversed abscissa with decreasing wave phases such that the diagnostics can be interpreted as east–west cross sections; wave phases 8–6 are located to the west (or ahead) of the rainfall peak, whereas wave phases 4–2 are located to the east (or behind) of the rainfall peak.

The composites show that observed and simulated inertio-gravity waves are associated with broad convergent flow in the lower troposphere near and west of the rainfall peak (phases 7–6) (Figs. 8a–c). Anomalous easterlies happen during much of the convectively active phase. Upper-tropospheric divergent flow happens over and to the east of the convectively active phase. The maximum IMERG precipitation rate anomalies and the maximum ERA5 cloud anomalies happen near 5°N, and the amplitude of rainfall anomalies in the Southern Hemisphere is about half the amplitude of the Northern Hemisphere anomalies (Figs. 8a,d). This hemispheric asymmetry is also a reflection that these waves happen along the ITCZ, which is predominantly situated in the Northern Hemisphere.

All MPAS-A aquaplanet experiments capture a rainfall peak during phases 6–4, but the peak rainfall of MPAS-A (even in the 3-km experiment) is weaker than in the 20-yr IMERG climatology (Figs. 8b,c).

Resolved deep convection impacts the simulated structure of inertio-gravity waves. Heavier precipitation and more cloudiness are evident during the convectively active phase in the 3-km experiment than in the 15-km experiment (Figs. 8b,c,e,f). Rainfall and cloud anomalies simulated by the 3-km experiment are also more latitudinally confined than in the 15-km experiment; positive rainfall anomalies extend beyond 5°N/S in the 15-km experiment and cloud anomalies extend almost up to 10°N/S. Although all simulations yield similar circulation patterns, the upper-tropospheric divergent flow is more accurately positioned in the 3-km experiment (phases 4–3) than in the 15-km experiment (phases 5–4).

2) VERTICAL STRUCTURE

Most variables examined show a pronounced eastward tilt with height in both ERA5 and MPAS-A (Fig. 9). The temperature anomalies exhibit a "boomerang"-type pattern (Figs. 9a–c); pronounced cool anomalies appear in the lower to middle troposphere during phases 5–3, and those cool anomalies extend eastward with height until ~200 hPa where the cool anomalies extend westward trough the tropopause. The warm anomalies exhibit a similar pattern, except offset by 3–4 wave phases from the cool anomalies. Anomalous convergence, heating, and ascent begin in the lower troposphere during phases 5–7 (Figs. 9a–f). Upward motion, deep tropospheric heating, and upper-tropospheric divergence happen during the convectively active phase (Figs. 9a–f). Anomalous moist air exists between the surface and 700 hPa during phases 5–8; anomalous dry air exists over the same layer during phases 1–4 (Figs. 9g–i). While the water vapor mixing ratio anomalies exhibit two peaks (one at 750 hPa and another between 500 and 600 hPa), the relative humidity has a single peak in the upper troposphere possibly as a result of ice clouds. The magnitude of the anomalies is slightly stronger in MPAS-A than in ERA5, which could possibly be due to a stronger rainfall–circulation coupling in MPAS-A.

As in the composites of Kelvin waves, the vertical cross sections show key differences between the MPAS-A experiments (Fig. 9). The 3-km experiment is associated with weaker midtropospheric temperature anomalies but stronger upper-tropospheric temperature anomalies (Figs. 9b,c). This experiment is also associated with stronger heating, stronger convergence, and stronger ascent during the convectively active phase (Figs. 9e,f), as well as wetter conditions in the lower troposphere during phases 8–5 and in the middle troposphere during phases 5–3 (Figs. 9h,i). In the 15-km experiment, Q_1 and the water vapor mixing ratio exhibit an inflection below the melting level with parameterized convection (albeit less pronounced than for Kelvin waves). Such inflection is also evident in vertical profiles of averaged Q_1 during the convectively active phase (Fig. 10); Q_1 reaches a relative minimum of approximately 0.3 K day^{-1} at 675 hPa in both the 15- and 30-km experiments. At that
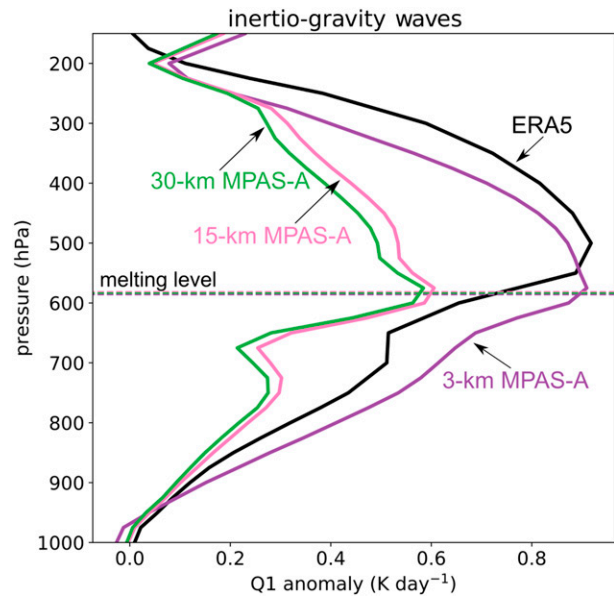

FIG. 10. As in Fig. 5, but for inertio-gravity waves.

same level, the 3-km experiment is associated with an average 0.76 K day^{-1} Q_1 anomaly, which is more than twice as strong as in the experiments with parameterized deep convection.

3) MSE BUDGET

Given the different three-dimensional structure of inertio-gravity waves across experiments, we also examined their maintenance and propagation with the MSE budget (Figs. 11a,b). Similar to Kelvin waves, the vertically integrated MSE budget shows strong agreement between the left- and right-hand sides of the MSE budget (Fig. S2 in the supplemental material). Inertio-gravity waves considered in this analysis are undergoing amplification—on average—in the 30-km experiment but dampening in the 15- and 3-km experiment (Fig. 11a). This difference is mostly due to the horizontal MSE advection, which aids wave amplification in the 30-km experiment and wave dampening in the 15- and 3-km experiment.

A noteworthy difference between experiments is the magnitude of contributions from the forcing terms (surface fluxes and radiative fluxes) to inertio-gravity waves maintenance (Fig. 11a). Surface fluxes are primary sources of inertio-gravity waves amplification when deep convection is resolved; their contributions are at least 4 times stronger in the 3-km experiment than in the 15-km experiment. This difference can be explained by the peak anomalous surface fluxes, which are twice as strong in the 3-km experiment as in the 15- and 30-km experiment (Fig. S2). The leading role of surface fluxes is consistent with observations because these waves happen on a quasi-2-day period through a combination of diurnal forcing on the first day and strong boundary layer recovery through surface heat fluxes on the second day (Chen and Houze 1997; Yu et al. 2018). CRI also contribute to wave amplification in the 15- and 3-km experiments, but their contributions to inertio-gravity waves maintenance are much smaller in comparison to Kelvin waves. Last, the
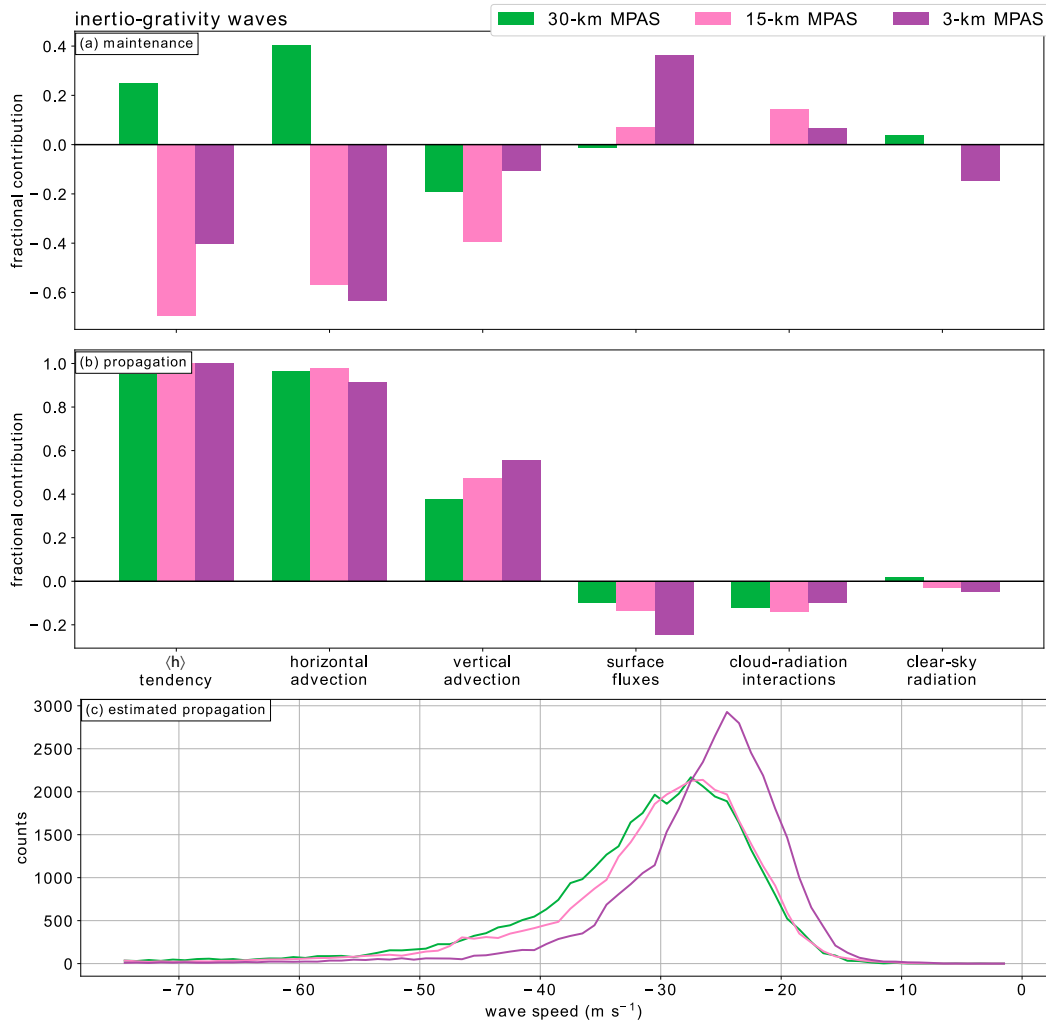
FIG. 11. As in Fig. 6, but for inertio-gravity waves. Negative values represent westward propagation.

contributions from CLEAR vary across all experiments—from amplifying the waves in the 30-km experiment to dampening the waves in the 3-km experiment.

All experiments show consistent mechanisms driving the propagation of inertio-gravity waves (Fig. 11b). Horizontal MSE advection contributes the most to wave propagation; this term alone contributes more than 100% of the full tendency. Vertical MSE advection also plays a substantial role in propagating the waves, whereas all other terms retard the waves. It is intriguing that surface fluxes and CRI aid wave amplification, but the same terms slow down the propagation of inertio-gravity waves. The most evident differences between experiments are the larger magnitudes of both vertical MSE advection and surface fluxes in the 3-km experiment.

Despite the consistent propagation mechanisms, the experiments show different propagation speeds (Fig. 11c; negative values represent westward propagation). Inertio-gravity waves propagate at slower speeds with resolved deep convection. The distribution from the 3-km experiment is skewed toward lower values, resulting in average speeds of -25 m s^{-1} in this experiment and ~ 30 m s^{-1} in the experiments with parameterized convection. Both speeds are within the range of estimated propagation speeds as estimated from observations (Takayabu 1994; Kiladis et al. 2009). The slower propagation speeds in the 3-km experiment could stem from the stronger retardation by surface fluxes when deep convection is resolved (Fig. 11b), although a more detailed analysis is needed to confirm this possibility.

c. Easterly waves

1) RAINFALL, CLOUDS, AND HORIZONTAL STRUCTURE

Of the three CCEWs examined, easterly waves exhibit the largest discrepancies between ERA5/IMERG and the MPAS-A aquaplanet experiments. The 20-yr composite from IMERG shows an asymmetric rainfall structure with peak anomalies between 2.5° and 5°N (Fig. 12a). This is expected because easterly waves are most active during boreal summer (Serra and Houze 2002; Kiladis et al. 2006; Serra et al. 2008;
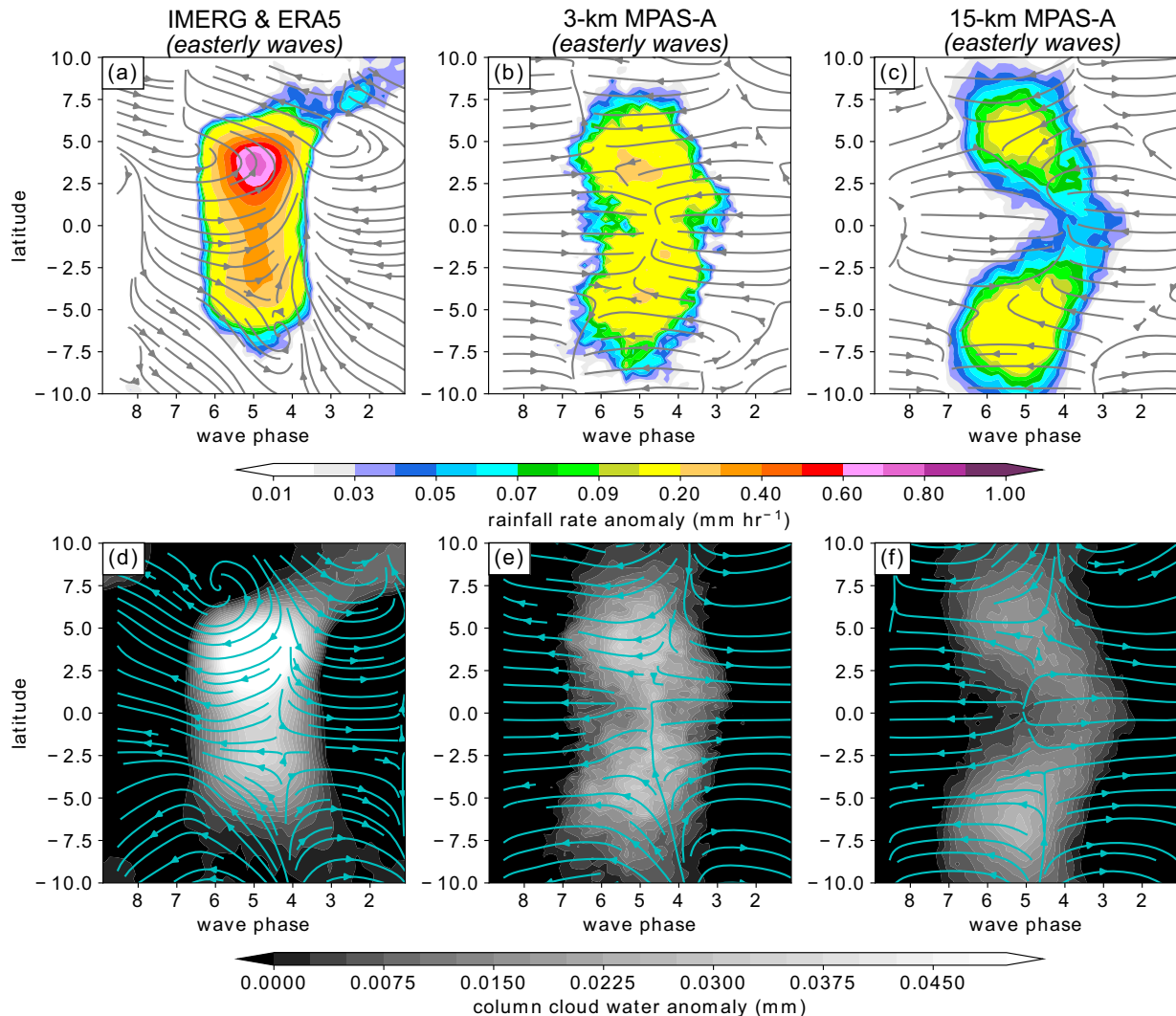
FIG. 12. As in Fig. 3, but for easterly waves.

Rydbeck and Maloney 2014; Dominguez et al. 2020; Feng et al. 2020a,c). The ERA5 composite shows lower-tropospheric westerlies over most of the anomalous rainfall as well as a trough just to the west of the rainfall peak (phases 8–6). Positive rainfall and cloud anomalies extend northeastward and southward of the rainfall peak (Figs. 12a,d). In contrast, MPAS-A simulates weaker easterly waves with nearly hemispheric symmetric rainfall and cloud anomalies (Figs. 12b,c,e,f). The 3-km experiment produces a nearly continuous rainfall shield across the equator, while the 15-km experiment has two anomalies separated by a local minimum at the equator. Both experiments hint at the presence of lower-tropospheric cyclonic gyres in each hemisphere—this structure is more similar, although not exactly the same, to the expected structure of equatorial Rossby waves (Kiladis et al. 2009). Despite these differences, both ERA5 and MPAS-A show upper-tropospheric divergent flow that results from anomalous westerlies over and west of the rainfall peak and anomalous easterlies to the east (Figs. 12d–f).

We have two hypotheses for the contrasting horizontal rainfall and lower-tropospheric kinematic structure of observed and simulated easterly waves. The first hypothesis is that easterly waves are sensitive to the underlying SST profile, the base state, and possibly other factors that are limited by the aquaplanet configuration. The second hypothesis is that other disturbances are aliasing into the wavenumber–frequency space of easterly waves; Nakajima et al. (2013) also noted this hypothesis. A future study should investigate these two hypotheses by, for example, evaluating the structure of easterly waves in aquaplanet experiments with hemispheric asymmetric SST profiles that can more closely resemble summertime conditions (when these waves are most active).

Resolved deep convection primarily affects the rainfall and lower-tropospheric winds of easterly waves in the aquaplanet framework. Rainfall anomalies appear collocated with cyclonic circulations on each hemisphere, and the center of those circulations is closer to the equator in the 3-km experiment than in the 15-km experiment (Figs. 12b,c). Consequently, the rainfall
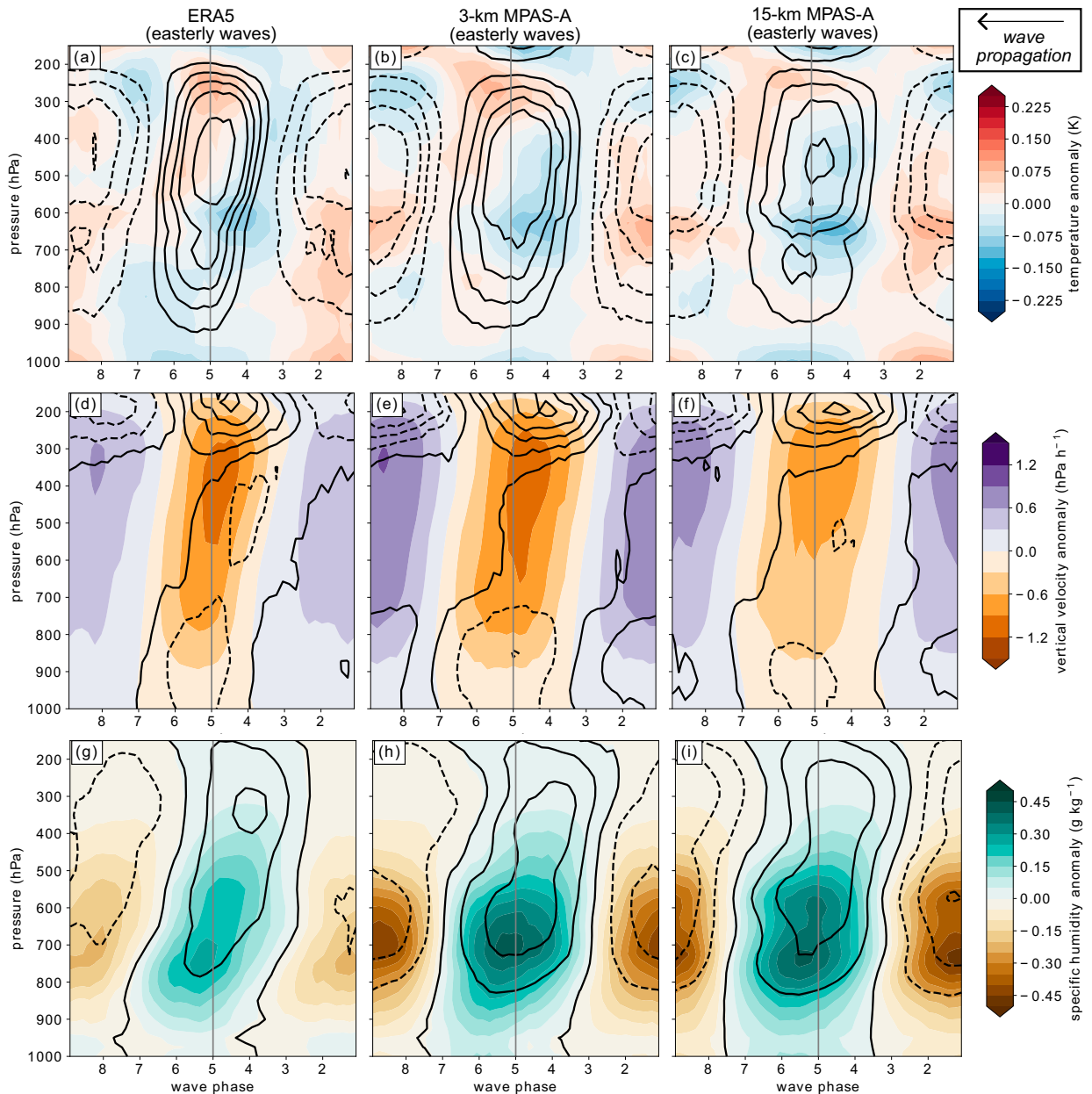
FIG. 13. As in Fig. 4, but for except for easterly waves.

anomalies extend nearly continuously from 10°S to 10°N in the 3-km experiment, but there is a gap in rainfall anomalies at the equator in the 15-km experiment. This result likely stems from the different mean states of these simulations; Rios-Berrios et al. (2022) showed that the experiment with resolved convection yields a stronger and narrower ITCZ than the experiments with parameterized deep convection.

2) VERTICAL STRUCTURE

The vertical cross sections reveal similarities between easterly waves in ERA5 and MPAS-A—despite their different

lower-tropospheric horizontal structure (Figs. 13). Both sources exhibit cool and warm anomalies through the troposphere during the convectively active phase (Figs. 13a–c), but their magnitudes are comparably weaker to the temperature anomalies associated with Kelvin and inertio-gravity waves. Deep tropospheric heating and anomalous ascent are evident during phases 6–3, with peak anomalous heating and ascent between 300 and 600 hPa (Figs. 13a–f). Lower-tropospheric convergence and upper-tropospheric divergence both happen during phases 6–4 (Figs. 13d–f). Likewise, anomalous moist conditions exist over those phases with peak water vapor mixing ratio between 700 and 800 hPa during phase 5 and peak relative

humidity anomalies around 500 hPa between phases 5 and 3 (Figs. 13g–i). The prominent water vapor anomalies in these waves support their classification as moisture modes (Adames et al. 2019).

Consistent with the horizontal maps, the biggest differences between the cross sections of ERA5 and MPAS-A appear in the lower troposphere. Easterly waves in ERA5 are associated with eastward tilted cool and moist anomalies between 900 and 700 hPa during phases 7–4 (Figs. 13g). MPAS-A shows a more barotropic structure and even has weak warm anomalies during those phases (Figs. 13h,i). Additionally, ERA5 also shows stronger lower-tropospheric convergence and ascent than the aquaplanet experiments between phases 7 and 4 (Figs. 13d–i). These discrepancies further suggest that either the aquaplanet framework is missing key processes that modulate the lower-tropospheric structure of Pacific easterly waves or that other disturbances are aliasing into the easterly wavenumber–frequency space.

Resolved deep convection affects the strength of these waves and their associated anomalies. The 3-km experiment produces stronger anomalous heating, ascent, and lower-tropospheric convergence than the 15-km experiment (Figs. 13b,c,e,f). These waves are also associated with weaker cool and warm anomalies near 675 and 1000 hPa with resolved convection (Figs. 13b,c). Within that level, Q_1 exhibits a relative minimum of about 0.5 K day^{-1} during the convectively active phase when deep convection is parameterized (Fig. 14); there is no relative minimum in the 3-km experiment. Yet, all experiments exhibit comparable moist anomalies during phases 7–4 without a discontinuity below the melting level as was noted for Kelvin and inertio-gravity waves (Figs. 13h,i).

3) MSE BUDGET

The aforementioned results motivated the analysis of maintenance and propagation mechanisms for easterly waves. The primary purpose is to investigate if those mechanisms exhibit any major discrepancies between experiments given that the structural differences are comparatively smaller than for the other waves considered. Figures 15a and 15b show this analysis based on the vertically integrated MSE budget. The individual terms of the budget are shown in Fig. S3; there is also good agreement between the sum of the calculated terms and the actual tendency of $\langle h \rangle$.

The main difference between experiments is the magnitude of each contributing process to wave amplification or dampening (Fig. 15a). CRI and CLEAR aid wave amplification, whereas the advective processes dampen the easterly waves in all experiments. The contributions from horizontal MSE advection generally increase with decreasing cell spacing, whereas the contributions from vertical advection and radiative fluxes decrease in magnitude with decreasing grid spacing. Surface fluxes exhibit the most dramatic difference between experiments; while this term has nearly negligible contribution to amplification in the 3-km experiment, this term dampens the easterly waves in the 15- and 30-km experiment. This contrasting contribution is a result of near-surface winds at the equator because the 30- and 15-km experiments have anomalous
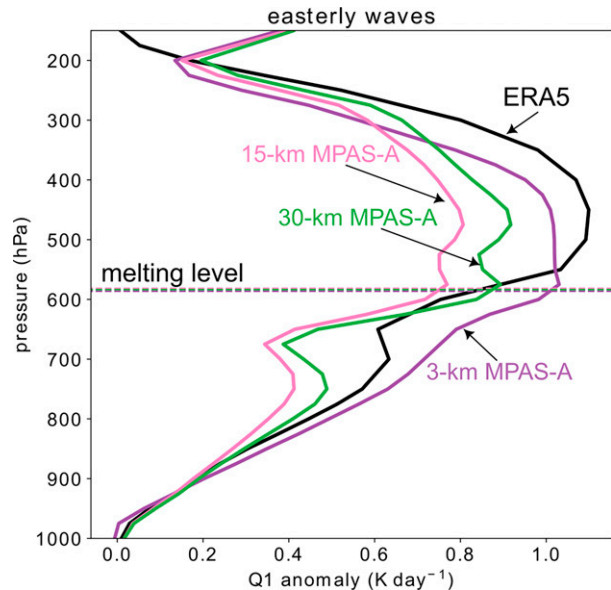

FIG. 14. As in Fig. 5, but for easterly waves.

westerlies between the two rainfall anomalies (Figs. 15b,c), which combined with background easterlies results in anomalously total weak winds and weak surface fluxes.

Horizontal MSE advection contributes the most to easterly waves propagation in all experiments (Fig. 15b). All other processes are associated with nearly negligible contributions. Vertical MSE advection also aids wave propagation, whereas surface fluxes and CRI retard the easterly waves in MPAS-A. These results imply that easterly waves in the aquaplanet framework are largely advected by the mean flow. This result is consistent with the westward-propagating Rossby-like wave signal identified by Mayta et al. (2022).

Even though the contributions to wave propagation are similar across all experiments, easterly waves propagate slightly faster in the 3-km experiment (Fig. 15c). The distribution of wave speeds from the 3-km experiment is skewed toward more negative values (implying a faster westward propagation) in comparison to the 30- and 15-km experiments. The mean propagation speed of easterly waves is -11, -10.5, and -9 m s^{-1} in the 3-, 15-, and 30-km experiments, respectively. Given the dominant role of horizontal MSE advection on wave propagation, this result implies that resolved deep convection yields either stronger easterlies or stronger zonal MSE gradients that aid faster propagation than in the experiments with parameterized deep convection.

4. Summary and conclusions

This study examined the simulated three-dimensional structure of CCEWs in the MPAS-A model with parameterized or resolved deep convection. Kelvin waves, inertio-gravity waves, and easterly waves from three MPAS-A aquaplanet experiments were compared against a 20-yr climatology of those waves over the Pacific Ocean. The comparison shows that all MPAS-A experiments capture the overall horizontal
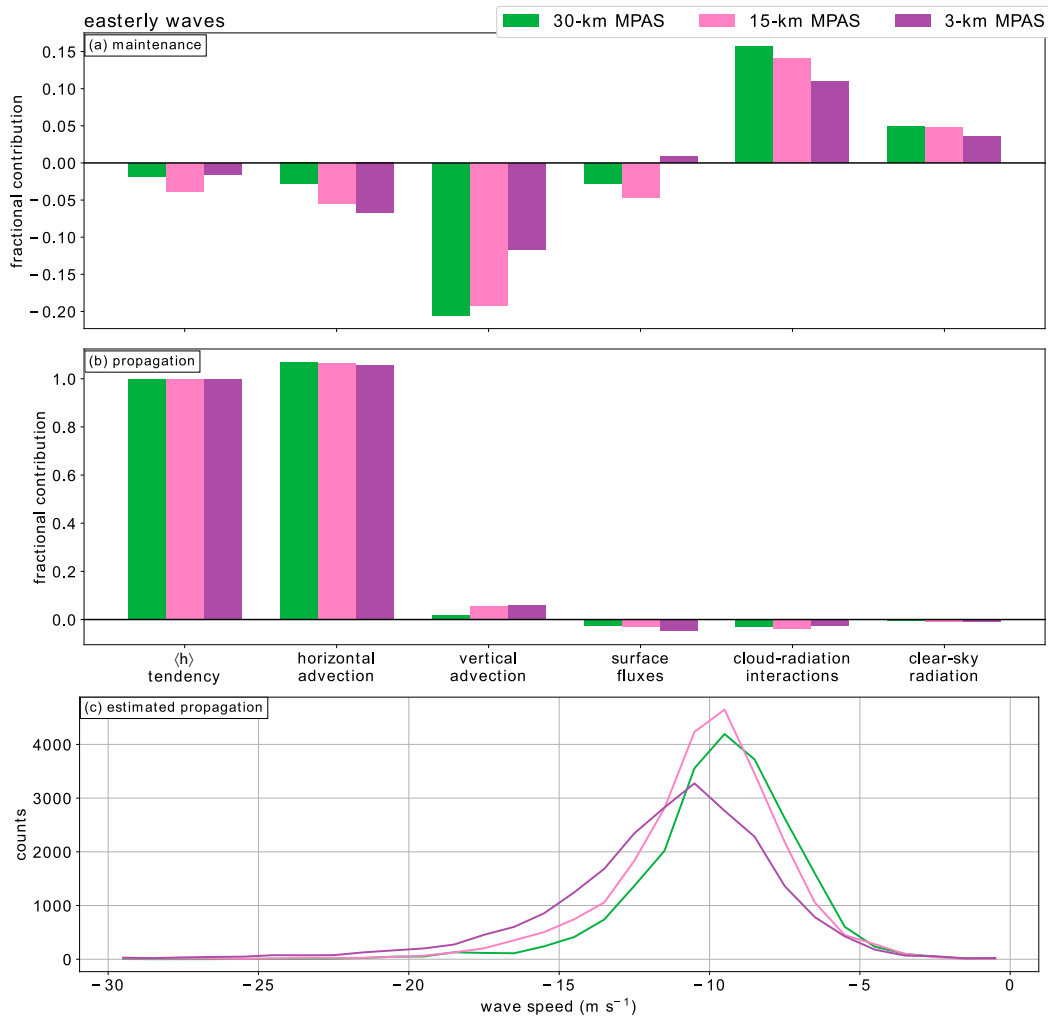
FIG. 15. As in Fig. 6, but for easterly waves. Negative values represent westward propagation.

and vertical structure of Kelvin and inertio-gravity waves regardless of horizontal resolution. An intercomparison of those experiments showed that resolved convection yields stronger waves that are associated with stronger anomalous ascent, diabatic heating, lower-tropospheric convergence, and upper-tropospheric divergence than with parameterized deep convection. Importantly, the experiment with resolved deep convection also produces weaker temperature anomalies between 600 and 700 hPa, which is around and below the melting level in the simulations. The apparent heat source (Q_1) shows a relative minimum around those levels only when deep convection is parameterized. This result suggests that the convection parameterization (Tiedtke) is producing too much melting. The different Q_1 profiles, and the associated temperature and moisture anomalies, affect the maintenance and propagation of Kelvin and inertio-gravity waves as documented with an MSE budget. Both of these wave groups propagate at slower speed when deep convection is explicitly resolved.

Resolved deep convection appears to have the strongest impact on gravity wave–type equatorial waves. Kelvin waves and inertio-gravity waves both exhibited key differences in their vertical structure between parameterized and resolved deep convection, but easterly waves were strikingly similar between experiments. Although more research is needed, it is possible that resolved deep convection affects both the temperature and moisture perturbations that are critical for gravity wave–type waves (Wolding et al. 2020). The effects on moisture-mode-type waves could be less pronounced because those waves are less sensitive to temperature perturbations. The main difference between simulated easterly waves was the strength of their anomalies; the experiment with resolved deep convection captured stronger rainfall anomalies associated with stronger ascent, diabatic heating, surface heat fluxes, lower-tropospheric convergence, and upper-tropospheric divergence. These effects of resolved deep convection on moisture mode–type waves stem from a better moisture–rainfall relationship (see Fig. 11 from Rios-Berrios et al. 2022). Easterly

waves also propagate faster when deep convection is resolved, likely due to stronger horizontal advection by the background flow.

Unlike Kelvin and inertio-gravity waves, easterly waves in the aquaplanet experiments differed substantially from their observed counterparts. Their associated rainfall and lower-tropospheric rainfall anomalies resemble more observed equatorial Rossby waves than easterly waves. The lower-tropospheric temperature anomalies showed anomalously cool air to the west of the wave peak in ERA5, whereas there is anomalously warm air in the aquaplanet experiments. These differences are mostly confined to the lower troposphere as the upper-tropospheric structure was similar between ERA5 and the aquaplanet experiments. Observed easterly waves primarily happen during boreal summer and fall; therefore, the aquaplanet configuration with symmetric SST and perpetual equinoctial conditions may not be adequate to capture the key lower-tropospheric features and jets that characterize east Pacific and west Pacific easterly waves.

We recognize that this study is limited because we used an aquaplanet framework with fixed and hemispheric symmetric SSTs. While we tried to overcome that limitation by comparing the simulated CCEWs against reanalysis and satellite data of CCEWs over the Pacific Ocean, additional research is needed to confirm the applicability of our findings to real-data NWP model simulations. Another limitation of our study is the use of a single-moment microphysics scheme. Studies have shown that single-moment microphysics schemes, while less computationally expensive than double-moment microphysics, produce excessive rainwater evaporation (e.g., Bryan and Morrison 2012; Igel et al. 2015), which could affect the simulated structure of CCEWs. Although we demonstrate that the experiments with parameterized convection produce *too much cooling* near and below the melting level, we have yet to confirm that the experiment with resolved convection is not producing *too much heating* in that region. Future work should address these limitations by, e.g., investigating the accuracy of CCEWs structure in more complex models with resolved deep convection and preferably double moment microphysics. If the results presented here are confirmed, they would point at improvements in the representation of processes around the melting level as a possible venue for improved forecasts of CCEWs and tropical rainfall variability.

Data availability statement. The numerical model simulations upon which this study is based are too large to archive or to transfer. Instead, we provide postprocessed model output (Rios-Berrios et al. 2020a). Additionally, the model code with modifications to use the aquaplanet framework, compilation script, initial condition files, and the namelist settings are documented in Jacobsen et al. (2022).

REFERENCES

Adames, Á. F., and J. M. Wallace, 2015: Three-dimensional structure and evolution of the moisture field in the MJO. *J. Atmos. Sci.*, **72**, 3733–3754, https://doi.org/10.1175/JAS-D-15-0003.1.

——, D. Kim, S. K. Clark, Y. Ming, and K. Inoue, 2019: Scale analysis of moist thermodynamics in a simple model and the relationship between moisture modes and gravity waves. *J. Atmos. Sci.*, **76**, 3863–3881, https://doi.org/10.1175/JAS-D-19-0121.1.

Ahmed, F., J. D. Neelin, and Á. F. Adames, 2021: Quasi-equilibrium and weak temperature gradient balances in an equatorial beta-plane model. *J. Atmos. Sci.*, **78**, 209–227, https://doi.org/10.1175/JAS-D-20-0184.1.

Andersen, J. A., and Z. Kuang, 2012: Moist static energy budget of MJO-like disturbances in the atmosphere of a zonally symmetric aquaplanet. *J. Climate*, **25**, 2782–2804, https://doi.org/10.1175/JCLI-D-11-00168.1.

Benedict, J. J., B. Medeiros, A. C. Clement, and J. G. Olson, 2020: Investigating the role of cloud-radiation interactions in subseasonal tropical disturbances. *Geophys. Res. Lett.*, **47**, e2019GL086817, https://doi.org/10.1029/2019GL086817.

Berry, G., and M. J. Reeder, 2014: Objective identification of the intertropical convergence zone: Climatology and trends from the ERA-Interim. *J. Climate*, **27**, 1894–1909, https://doi.org/10.1175/JCLI-D-13-00339.1.

Blackburn, M., and B. J. Hoskins, 2013: Context and aims of the aqua-planet experiment. *J. Meteor. Soc. Japan*, **91A**, 1–15, https://doi.org/10.2151/jmsj.2013-A01.

——, and Coauthors, 2013: The aqua-planet experiment (APE): Control SST simulation. *J. Meteor. Soc. Japan*, **91A**, 17–56, https://doi.org/10.2151/jmsj.2013-A02.

Blanco, J. E., D. S. Nolan, and S. N. Tulich, 2016a: Convectively coupled Kelvin waves in aquachannel simulations: 1. Propagation speeds, composite structures, and comparison with aquaplanets. *J. Geophys. Res. Atmos.*, **121**, 11 287–11 318, https://doi.org/10.1002/2016JD025004.

——, ——, and B. E. Mapes, 2016b: Convectively coupled Kelvin waves in aquachannel simulations: 2. Life cycle and dynamical-convective coupling. *J. Geophys. Res. Atmos.*, **121**, 11 319–11 347, https://doi.org/10.1002/2016JD025022.

Bryan, G. H., and H. Morrison, 2012: Sensitivity of a simulated squall line to horizontal resolution and parameterization of microphysics. *Mon. Wea. Rev.*, **140**, 202–225, https://doi.org/10.1175/MWR-D-11-00046.1.

Chen, S. S., and R. A. Houze Jr., 1997: Diurnal variation and life-cycle of deep convective systems over the tropical Pacific warm pool. *Quart. J. Roy. Meteor. Soc.*, **123**, 357–388, https://doi.org/10.1002/qj.49712353806.

Dias, J., M. Gehne, G. N. Kiladis, N. Sakaeda, P. Bechtold, and T. Haiden, 2018: Equatorial waves and the skill of NCEP and ECMWF numerical weather prediction systems. *Mon. Wea. Rev.*, **146**, 1763–1784, https://doi.org/10.1175/MWR-D-17-0362.1.

Dominguez, C., J. M. Done, and C. L. Bruyère, 2020: Easterly wave contributions to seasonal rainfall over the tropical Americas in observations and a regional climate model.

Climate Dyn., **54**, 191–209, https://doi.org/10.1007/s00382-019-04996-7.

Feng, T., X.-Q. Yang, J.-Y. Yu, and R. Huang, 2020a: Convective coupling in tropical-depression-type waves. Part I: Rainfall characteristics and moisture structure. *J. Atmos. Sci.*, **77**, 3407–3422, https://doi.org/10.1175/JAS-D-19-0172.1.

——, J.-Y. Yu, X.-Q. Yang, and R. Huang, 2020b: Convective coupling in tropical-depression-type waves. Part II: Moisture and moist static energy budgets. *J. Atmos. Sci.*, **77**, 3423–3440, https://doi.org/10.1175/JAS-D-19-0173.1.

Frank, W. M., and P. E. Roundy, 2006: The role of tropical waves in tropical cyclogenesis. *Mon. Wea. Rev.*, **134**, 2397–2417, https://doi.org/10.1175/MWR3204.1.

Frierson, D. M. W., 2007: Convectively coupled Kelvin waves in an idealized moist general circulation model. *J. Atmos. Sci.*, **64**, 2076–2090, https://doi.org/10.1175/JAS3945.1.

——, D. Kim, I.-S. Kang, M.-I. Lee, and J. Lin, 2011: Structure of AGCM-simulated convectively coupled Kelvin waves and sensitivity to convective parameterization. *J. Atmos. Sci.*, **68**, 26–45, https://doi.org/10.1175/2010JAS3356.1.

Gill, A. E., 1980: Some simple solutions for heat-induced tropical circulation. *Quart. J. Roy. Meteor. Soc.*, **106**, 447–462, https://doi.org/10.1002/qj.49710644905.

Hersbach, H., and Coauthors, 2020: The ERA5 global reanalysis. *Quart. J. Roy. Meteor. Soc.*, **146**, 1999–2049, https://doi.org/10.1002/qj.3803.

Hong, S.-Y., J. Dudhia, and S.-H. Chen, 2004: A revised approach to ice microphysical processes for the bulk parameterization of clouds and precipitation. *Mon. Wea. Rev.*, **132**, 103–120, https://doi.org/10.1175/1520-0493(2004)132<0103:ARATIM>2.0.CO;2.

——, Y. Noh, and J. Dudhia, 2006: A new vertical diffusion package with an explicit treatment of entrainment processes. *Mon. Wea. Rev.*, **134**, 2318–2341, https://doi.org/10.1175/MWR3199.1.

Huffman, G. J., D. T. Bolvin, E. J. Nelkin, and J. Tan, 2019: Integrated Multi-satellitE Retrievals for GPM (IMERG) technical documentation. NASA Tech. Doc., 64 pp., https://gpm.nasa.gov/sites/default/files/document_files/IMERG_doc_190313.pdf.

Iacono, M. J., J. S. Delamere, E. J. Mlawer, M. W. Shephard, S. A. Clough, and W. D. Collins, 2008: Radiative forcing by long-lived greenhouse gases: Calculations with the AER radiative transfer models. *J. Geophys. Res.*, **113**, D13103, https://doi.org/10.1029/2008JD009944.

Igel, A. L., M. R. Igel, and S. C. van den Heever, 2015: Make it a double? Sobering results from simulations using single-moment microphysics schemes. *J. Atmos. Sci.*, **72**, 910–925, https://doi.org/10.1175/JAS-D-14-0107.1.

Jacobsen, D., and Coauthors, 2022: rosimarwx/MPAS-A_aquaplanet: MPAS-A v6.2 with modifications to use the aquaplanet capability. Zenodo, https://doi.org/10.5281/zenodo.6323189.

Johnson, R. H., P. E. Ciesielski, and T. M. Rickenbach, 2016: A further look at Q1 and Q2 from TOGA COARE. *Multiscale Convection-Coupled Systems in the Tropics: A Tribute to Dr. Michio Yanai, Meteor. Monogr.*, No. 56, Amer. Meteor. Soc., https://doi.org/10.1175/AMSMONOGRAPHS-D-15-0002.1.

Judt, F., and R. Rios-Berrios, 2021: Resolved convection improves the representation of equatorial waves and tropical rainfall variability in a global nonhydrostatic model. *Geophys. Res. Lett.*, **48**, e2021GL093265, https://doi.org/10.1029/2021GL093265.

——, and Coauthors, 2021: Tropical cyclones in global storm-resolving models. *J. Meteor. Soc. Japan*, **99**, 579–602, https://doi.org/10.2151/jmsj.2021-029.

Kiladis, G. N., C. D. Thorncroft, and N. M. J. Hall, 2006: Three-dimensional structure and dynamics of African easterly waves. Part I: Observations. *J. Atmos. Sci.*, **63**, 2212–2230, https://doi.org/10.1175/JAS3741.1.

——, M. C. Wheeler, P. T. Haertel, K. H. Straub, and P. E. Roundy, 2009: Convectively coupled equatorial waves. *Rev. Geophys.*, **47**, RG2003, https://doi.org/10.1029/2008RG000266.

Liu, Y., L. Guo, G. Wu, and Z. Wang, 2010: Sensitivity of ITCZ configuration to cumulus convective parameterizations on an aqua planet. *Climate Dyn.*, **34**, 223–240, https://doi.org/10.1007/s00382-009-0652-2.

Maloney, E. D., 2009: The moist static energy budget of a composite tropical intraseasonal oscillation in a climate model. *J. Climate*, **22**, 711–729, https://doi.org/10.1175/2008JCLI2542.1.

——, A. H. Sobel, and W. M. Hannah, 2010: Intraseasonal variability in an aquaplanet general circulation model. *J. Adv. Model. Earth Syst.*, **2**, 5, https://doi.org/10.3894/JAMES.2010.2.5.

Mayta, V. C., Á. F. Adames, and F. Ahmed, 2022: Westward-propagating moisture mode over the tropical western hemisphere. *Geophys. Res. Lett.*, **49**, e2022GL097799, https://doi.org/10.1029/2022GL097799.

Nakajima, K., Y. Yamada, Y. O. Takahashi, M. Ishiwatari, W. Ohfuchi, and Y.-Y. Hayashi, 2013: The variety of spontaneously generated tropical precipitation patterns found in APE results. *J. Meteor. Soc. Japan*, **91A**, 91–141, https://doi.org/10.2151/jmsj.2013-A04.

Nakamura, Y., and Y. N. Takayabu, 2022: Convective couplings with equatorial Rossby waves and equatorial Kelvin waves. Part I: Coupled wave structures. *J. Atmos. Sci.*, **79**, 247–262, https://doi.org/10.1175/JAS-D-21-0080.1.

Nasuno, T., H. Tomita, S. Iga, H. Miura, and M. Satoh, 2008: Convectively coupled equatorial waves simulated on an aquaplanet in a global nonhydrostatic experiment. *J. Atmos. Sci.*, **65**, 1246–1265, https://doi.org/10.1175/2007JAS2395.1.

Neale, R. B., and B. J. Hoskins, 2000: A standard test for AGCMs including their physical parametrizations: I: The proposal. *Atmos. Sci. Lett.*, **1**, 101–107, https://doi.org/10.1006/asle.2000.0022.

Riley, E. M., B. E. Mapes, and S. N. Tulich, 2011: Clouds associated with the Madden–Julian oscillation: A new perspective from *CloudSat*. *J. Atmos. Sci.*, **68**, 3032–3051, https://doi.org/10.1175/JAS-D-11-030.1.

Rios-Berrios, R., B. Medeiros, and G. H. Bryan, 2020a: Aquaplanet simulations using the model for prediction across scales (MPAS) version 6.2. UCAR/NCAR-GDEX, accessed 1 November 2021, https://doi.org/10.5065/cam1-v353.

——, ——, and ——, 2020b: Mean climate and tropical rainfall variability in aquaplanet simulations using the model for prediction across scales-atmosphere. *J. Adv. Model. Earth Syst.*, **12**, e2020MS002102, https://doi.org/10.1029/2020MS002102.

——, G. H. Bryan, B. Medeiros, F. Judt, and W. Wang, 2022: Differences in tropical rainfall in aquaplanet simulations with resolved or parameterized deep convection. *J. Adv. Model. Earth Syst.*, **14**, e2021MS002902, https://doi.org/10.1029/2021MS002902.

Roundy, P. E., 2008: Analysis of convectively coupled Kelvin waves in the Indian Ocean MJO. *J. Atmos. Sci.*, **65**, 1342–1359, https://doi.org/10.1175/2007JAS2345.1.

Rydbeck, A. V., and E. D. Maloney, 2014: Energetics of east Pacific easterly waves during intraseasonal events. *J. Climate*, **27**, 7603–7621, https://doi.org/10.1175/JCLI-D-14-00211.1.

Sakaeda, N., G. Kiladis, and J. Dias, 2020: The diurnal cycle of rainfall and the convectively coupled equatorial waves over

the Maritime Continent. *J. Climate*, **33**, 3307–3331, https://doi.org/10.1175/JCLI-D-19-0043.1.

Schlueter, A., A. H. Fink, P. Knippertz, and P. Vogel, 2019: A systematic comparison of tropical waves over northern Africa. Part I: Influence on rainfall. *J. Climate*, **32**, 1501–1523, https://doi.org/10.1175/JCLI-D-18-0173.1.

Schreck, C. J., III, 2015: Kelvin waves and tropical cyclogenesis: A global survey. *Mon. Wea. Rev.*, **143**, 3996–4011, https://doi.org/10.1175/MWR-D-15-0111.1.

Serra, Y. L., and R. A. Houze Jr., 2002: Observations of variability on synoptic timescales in the east Pacific ITCZ. *J. Atmos. Sci.*, **59**, 1723–1743, https://doi.org/10.1175/1520-0469(2002)059<1723:OOVOST>2.0.CO;2.

——, G. N. Kiladis, and M. F. Cronin, 2008: Horizontal and vertical structure of easterly waves in the Pacific ITCZ. *J. Atmos. Sci.*, **65**, 1266–1284, https://doi.org/10.1175/2007JAS2341.1.

Skamarock, W. C., J. B. Klemp, M. G. Duda, L. D. Fowler, S.-H. Park, and T. D. Ringler, 2012: A multiscale nonhydrostatic atmospheric model using centroidal Voronoi tesselations and C-grid staggering. *Mon. Wea. Rev.*, **140**, 3090–3105, https://doi.org/10.1175/MWR-D-11-00215.1.

Sobel, A., S. Wang, and D. Kim, 2014: Moist static energy budget of the MJO during DYNAMO. *J. Atmos. Sci.*, **71**, 4276–4291, https://doi.org/10.1175/JAS-D-14-0052.1.

Straub, K. H., and G. N. Kiladis, 2003: The observed structure of convectively coupled Kelvin waves: Comparison with simple models of coupled wave instability. *J. Atmos. Sci.*, **60**, 1655–1668, https://doi.org/10.1175/1520-0469(2003)060<1655:TOSOCC>2.0.CO;2.

——, P. T. Haertel, and G. N. Kiladis, 2010: An analysis of convectively coupled Kelvin waves in 20 WCRP CMIP3 global coupled climate models. *J. Climate*, **23**, 3031–3056, https://doi.org/10.1175/2009JCLI3422.1.

Takayabu, Y. N., 1994: Large-scale cloud disturbances associated with equatorial waves. *J. Meteor. Soc. Japan*, **72**, 451–465, https://doi.org/10.2151/jmsj1965.72.3_451.

van der Linden, R., A. H. Fink, J. G. Pinto, T. Phan-Van, and G. N. Kiladis, 2016: Modulation of daily rainfall in southern Vietnam by the Madden–Julian oscillation and convectively coupled equatorial waves. *J. Climate*, **29**, 5801–5820, https://doi.org/10.1175/JCLI-D-15-0911.1.

Ventrice, M. J., C. D. Thorncroft, and M. A. Janiga, 2012: Atlantic tropical cyclogenesis: A three-way interaction between an African easterly wave, diurnally varying convection, and a convectively coupled atmospheric Kelvin wave. *Mon. Wea. Rev.*, **140**, 1108–1124, https://doi.org/10.1175/MWR-D-11-00122.1.

Wang, W., 2022: Forecasting convection with a 'scale-aware' Tiedtke cumulus parameterization scheme at kilometer scales. *Wea. Forecasting*, **37**, 1491–1507, https://doi.org/10.1175/WAF-D-21-0179.1.

Weber, N. J., C. F. Mass, and D. Kim, 2020: The impacts of horizontal grid spacing and cumulus parameterization on subseasonal prediction in a global convection-permitting model. *Mon. Wea. Rev.*, **148**, 4747–4765, https://doi.org/10.1175/MWR-D-20-0171.1.

Wheeler, M., and G. N. Kiladis, 1999: Convectively coupled equatorial waves: Analysis of clouds and temperature in the wavenumber–frequency domain. *J. Atmos. Sci.*, **56**, 374–399, https://doi.org/10.1175/1520-0469(1999)056<0374:CCEWAO>2.0.CO;2.

Williamson, D. L., and Coauthors, 2013: The aqua-planet experiment (APE): Response to changed meridional SST profile. *J. Meteor. Soc. Japan*, **91A**, 57–89, https://doi.org/10.2151/jmsj.2013-A03.

Wolding, B., J. Dias, G. Kiladis, E. Maloney, and M. Branson, 2020: Interactions between moisture and tropical convection. Part II: The convective coupling of equatorial waves. *J. Atmos. Sci.*, **77**, 1801–1819, https://doi.org/10.1175/JAS-D-19-0226.1.

Yanai, M., S. Esbensen, and J.-H. Chu, 1973: Determination of bulk properties of tropical cloud clusters from large-scale heat and moisture budgets. *J. Atmos. Sci.*, **30**, 611–627, https://doi.org/10.1175/1520-0469(1973)030<0611:DOBPOT>2.0.CO;2.

Yasunaga, K., and B. Mapes, 2012: Differences between more divergent and more rotational types of convectively coupled equatorial waves. Part II: Composite analysis based on space–time filtering. *J. Atmos. Sci.*, **69**, 17–34, https://doi.org/10.1175/JAS-D-11-034.1.

Yu, H., R. H. Johnson, P. E. Ciesielski, and H.-C. Kuo, 2018: Observation of quasi-2-day convective disturbances in the equatorial Indian Ocean during DYNAMO. *J. Atmos. Sci.*, **75**, 2867–2888, https://doi.org/10.1175/JAS-D-17-0351.1.

Zhang, C., and Y. Wang, 2017: Projected future changes of tropical cyclone activity over the western North and South Pacific in a 20-km-mesh regional climate model. *J. Climate*, **30**, 5923–5941, https://doi.org/10.1175/JCLI-D-16-0597.1.